Automated discovery of interpretable hyperelastic material models for human brain tissue with EUCLID

Flaschel, Moritz; Yu, Huitian; Reiter, Nina; Hinrichsen, Jan; Budday, Silvia; Steinmann, Paul; Kumar, Siddhant; De Lorenzis, Laura

DOI
10.1016/j.jmps.2023.105404

Publication date
2023

Document Version
Final published version

Published in
Journal of the Mechanics and Physics of Solids

J. Mech. Phys. Solids 180 (2023) 105404

Contents lists available at ScienceDirect

Journal of the Mechanics and Physics of Solids

journal homepage: www.elsevier.com/locate/jmps

Automated discovery of interpretable hyperelastic material models for human brain tissue with EUCLID

Moritz Flaschel [a,1], Huitian Yu [a,1], Nina Reiter [b], Jan Hinrichsen [b], Silvia Budday [b], Paul Steinmann [b], Siddhant Kumar [c], Laura De Lorenzis [a,*]

[a] Department of Mechanical and Process Engineering, ETH Zürich, 8092 Zürich, Switzerland
[b] Department of Mechanical Engineering, Friedrich-Alexander-Universität of Erlangen–Nürnberg, 91058 Erlangen, Germany
[c] Department of Materials Science and Engineering, Delft University of Technology, 2628 CD Delft, The Netherlands

ARTICLE INFO

Dataset link: https://euclid-code.github.io/

Keywords:
Constitutive models
Hyperelasticity
Brain tissue
Interpretable models
Sparse regression

ABSTRACT

We propose an automated computational algorithm for simultaneous model selection and parameter identification for the hyperelastic mechanical characterization of biological tissue and validate it on experimental data stemming from human brain tissue specimens. Following the motive of the recently proposed computational framework EUCLID (Efficient Unsupervised Constitutive Law Identification and Discovery) and in contrast to conventional parameter calibration methods, we construct an extensive set of candidate hyperelastic models, i.e., a model library including popular models known from the literature, and develop a computational strategy for automatically selecting a model from the library that conforms to the available experimental data while being represented as an interpretable symbolic mathematical expression. This computational strategy comprises sparse regression, i.e., a regression problem that is regularized by a sparsity promoting penalty term that filters out irrelevant models from the model library, and a clustering method for grouping together highly correlated and thus redundant features in the model library. The model selection procedure is driven by data stemming from mechanical tests under different deformation modes, i.e., uniaxial compression/tension and simple torsion. The data is acquired through conventional mechanical tests that deliver labeled one-dimensional data pairs, and thus the method can be interpreted as a supervised counterpart to the originally proposed EUCLID that is informed by full-field displacement data and global reaction forces. The proposed method is verified on synthetical data with artificial noise. In addition, we present for the first time an experimental investigation of the EUCLID framework by validating the proposed method on experimental data acquired through mechanical tests of human brain specimens, proving that the method is capable of discovering hyperelastic models that exhibit both high fitting accuracy to the data as well as concise and thus interpretable mathematical representations.

1. Introduction

Despite extensive research over the past decades, the characterization of the mechanical response of biological tissues like those of the human brain remains an active field with many open questions, see the review article by Budday et al. (2020). The amount

* Corresponding author.
E-mail address: ldelorenzis@ethz.ch (L. De Lorenzis).
[1] These authors contributed equally.

https://doi.org/10.1016/j.jmps.2023.105404
Received 3 May 2023; Received in revised form 28 June 2023; Accepted 2 August 2023
Available online 9 August 2023

of data is usually limited by ethical restrictions and by the availability of only few specimens with short durability (Faber et al., 2022). The general objective is therefore to leverage these limited data in an efficient manner to discover an adequate mathematical description of the tissue response. The conventional strategy is to a priori assume a constitutive model and to calibrate the tunable model parameters by means of the experimental measurements. However, the a priori choice of the constitutive model is driven by human experience and intuition; thus, this classical strategy is highly susceptible to introducing modeling errors that lead to poor fitting accuracy and/or the need for tedious and time-consuming iterative model correction procedures. Data-driven methods and machine learning approaches promise a powerful remedy. In this work, one of such methods, which falls under the umbrella of methods denoted as EUCLID (Efficient Unsupervised Constitutive Law Identification and Discovery) (Flaschel et al., 2021), is used for automatically discovering symbolic expressions of hyperelastic material models for human brain tissue based on experimental measurements.

The general idea behind machine-learning-based material modeling is to choose a model ansatz that exhibits a high expressiveness owing to a vast amount of tunable parameters, and to calibrate these parameters by leveraging the available data. Popular examples of versatile machine-learning-based material models include neural networks (Ghaboussi et al., 1991), splines (Sussman and Bathe, 2009), Gaussian processes (Frankel et al., 2020), and neural ordinary differential equations (Tac et al., 2022). In the context of hyperelasticity, these methods can be used to learn the characteristic strain energy density function while special attention needs to be attributed to not violating physical constraints like objectivity or (poly-)convexity of the strain energy density function (As'ad et al., 2022; Klein et al., 2022a,b; Kalina et al., 2022; Thakolkaran et al., 2022; Chen and Guilleminot, 2022; Linka and Kuhl, 2022; As'ad and Farhat, 2022; Tac et al., 2022). Until now, the majority of the proposed machine learning models for hyperelasticity are informed by artificially generated data, e.g., data generated through simulations at the microscopic level. Exceptions are for example the works by Linka et al. (2021, 2023), who train neural networks based on real experimental data for the characterization of human brain tissue. In contrast to machine-learning-based approaches stand model-free data-driven methods (Kirchdoerfer and Ortiz, 2016; Ibañez et al., 2018), which seek to avoid the formulation of a material model altogether by solving forward problems that are directly informed by the data.

Both the previously mentioned machine-learning-based approaches as well as model-free data-driven methods have in common that the constitutive behavior is encoded in a black box that does not allow for physical interpretation, e.g., it is difficult to interpret the meaning of the many functions and parameters that compose models encoded in machine learning tools like neural networks. Furthermore, these methods typically rely on a vast amount of labeled data pairs that are not available under experimental conditions. The recognition of these issues motivated the development of the EUCLID method, which aims to leverage sparse regression (Frank and Friedman, 1993; Tibshirani, 1996; Efron et al., 2004; Friedman et al., 2010) to discover interpretable symbolic expressions of material models using only experimentally available data like displacement fields and global reaction forces. Initially applied to hyperelasticity (Flaschel et al., 2021; Joshi et al., 2022) (see also the related and independent work by Wang et al. (2021)), the framework was later extended to viscoelasticity (Marino et al., 2023), elastoplasticity (Flaschel et al., 2022), and generalized standard materials (Flaschel et al., 2023), see Flaschel (2023) for an overview. Recently, discovering symbolic expressions for material models is gaining more and more attention in the field, see, e.g., the works by Bomarito et al. (2021), Kabliman et al. (2021), Park and Cho (2021), Abdusalamov et al. (2023), Meyer and Ekre (2023), Linka et al. (2023) and St. Pierre et al. (2023). Similar to the philosophy of EUCLID, the recent works by Linka et al. (2023) and St. Pierre et al. (2023) combine the ideas of versatile neural networks with a sparsity promoting regularization term for learning strain energy density functions of hyperelastic tissue with a small amount of nonzero parameters. These authors treat the problem with gradient-based optimizers that are commonly used to train neural networks, and hence do not utilize highly efficient solvers for sparse regression problems as those proposed by Efron et al. (2004) and Friedman et al. (2010).

In this work, EUCLID is used to automatically discover hyperelastic strain energy density functions for describing the mechanical behavior of human brain tissue. The idea is to construct a set of candidate material models called the model library, which can be assembled for example from the vast available literature on hyperelastic material models (see the non-comprehensive list of reviewing articles by Boyce and Arruda (2000), Marckmann and Verron (2006), Steinmann et al. (2012), Dal et al. (2021) and He et al. (2021)), and to use a specifically designed algorithm, based on sparse regression (Tibshirani, 1996) and feature clustering, to select from the library a material model which is encoded by an interpretable, simple mathematical expression and which is able to well capture the mechanical behavior observed in the experimental data. Unlike in previously proposed sparse-regression-based methods in the field (Flaschel et al., 2021; Wang et al., 2021), here the library of material models also contains models that depend nonlinearly on the material parameters. Due to the wet and shiny surface of brain tissues, displacement field data are difficult to acquire; thus, against the original philosophy of EUCLID (Flaschel, 2023), the method in this paper is not informed by full-field displacement and global reaction force data. Instead, we rely here on one-dimensional labeled data pairs stemming from uniaxial compression/tension and simple torsion tests of human brain tissue specimens.

The paper is organized as follows: In Section 2, we construct the model library in which EUCLID searches for a suitable material model. In Section 3, the proposed algorithm for model selection is discussed in detail. Subsequently, the method is tested on artificial data and actual experimental data in Sections 4 and 5, respectively, and conclusions are drawn in Section 6.

Notation: Tensors and matrices may appear in compact or index notation, e.g., $\mathbf{F}$ or F_{ij}, respectively. In compact notation, first-order tensors (vectors) and second-order tensors are denoted by bold letters, e.g., $\mathbf{F}$. The transpose of a tensor is denoted by $\square^T$. When appearing in index notation, the order of the tensor equals the number of the indices. If not stated otherwise, the Einstein convention for summation over repeated indices is used in equations appearing in index notation, e.g., $a_i b_i = \sum_i a_i b_i$. Inner products are denoted by $\cdot$, e.g., $\boldsymbol{a} \cdot \boldsymbol{b} = a_i b_i$, and outer products by $\otimes$, e.g., $\{\boldsymbol{a} \otimes \boldsymbol{b}\}_{ij} = a_i b_j$. If no operation is indicated between two tensors, the juxtaposition implies tensor contraction, e.g., $\{\mathbf{F}^T\mathbf{F}\}_{ij} = F_{ki}F_{kj}$. The trace of a tensor is denoted by $\mathrm{tr}(\square)$, e.g., $\mathrm{tr}(\mathbf{C}) = C_{ii}$, the volumetric part by $\mathrm{vol}(\square)$, the deviatoric part by $\mathrm{dev}(\square)$, and the determinant by $\det(\square)$.

2. Model library

2.1. Strain energy density

The constitutive response of a hyperelastic material is completely characterized by the material strain energy density function. In the spirit of EUCLID, we construct a material model library, i.e., a large set of potential candidate material models, by introducing a general parametric ansatz for the unknown strain energy density. Under the assumption of incompressibility, the strain energy density W of a hyperelastic material is postulated as (Holzapfel, 2000)

$$W = \tilde{W}(\mathbf{F}) - p \cdot (J - 1), \tag{1}$$

where $\mathbf{F}$ is the deformation gradient, p is a scalar Lagrange multiplier that can be physically interpreted as the hydrostatic (or volumetric) pressure, and $J = \det \mathbf{F} \overset{!}{=} 1$ is the determinant of the deformation gradient. A sufficient condition to satisfy the objectivity requirement for the material model is that W depends on $\mathbf{F}$ through the right Cauchy–Green tensor $\mathbf{C} = \mathbf{F}^T\mathbf{F}$, i.e. $\tilde{W}(\mathbf{F}) = \hat{W}(\mathbf{C})$. Assuming furthermore isotropic material behavior, the contribution $\hat{W}$ can be expressed as a function of the invariants of $\mathbf{C}$, defined as $I_1 = \mathrm{tr}(\mathbf{C})$, $I_2 = \frac{1}{2}(\mathrm{tr}^2(\mathbf{C}) - \mathrm{tr}(\mathbf{C}^2))$ and $I_3 = \det(\mathbf{C})$. An equally objective possibility for isotropic hyperelasticity is to express the strain energy density as a function of the principal stretches λ_1, λ_2, λ_3 defined as the eigenvalues of the right stretch tensor $\mathbf{U}$, which in turn is defined through the polar decomposition $\mathbf{F} = \mathbf{RU}$ (Holzapfel, 2000). As we seek to avoid a priori assumptions on the material response, we do not limit ourselves to a strain energy density that depends solely on the strain invariants or solely on the principal stretches, but instead consider the general case in which the strain energy density includes a contribution $\tilde{W}_I$ that depends on the strain invariants and a contribution $\tilde{W}_\lambda$ that depends on the principal stretches

$$W = \tilde{W}_I(I_1, I_2, I_3) + \tilde{W}_\lambda(\lambda_1, \lambda_2, \lambda_3) - p \cdot (J - 1). \tag{2}$$

By doing so, we obtain a highly general expression for the strain energy density that encompasses many well-known hyperelastic constitutive models e.g. of the Mooney–Rivlin or Ogden types.

To introduce a general parametric ansatz for $\tilde{W}_I$, we assume that it can be expressed as a linear combination of a priori chosen nonlinear feature functions

$$\tilde{W}_I(I_1, I_2, I_3) = \boldsymbol{\theta}_I \cdot \boldsymbol{Q}_I(I_1, I_2, I_3), \tag{3}$$

where the nonlinear feature functions have been collected in the vector $\boldsymbol{Q}_I$ and $\boldsymbol{\theta}_I$ is a vector of unknown real-valued material parameters. We construct the feature vector $\boldsymbol{Q}_I$ such that it contains features of the generalized Mooney–Rivlin model (Rivlin, 1947) and a logarithmic feature as it appears in the Gent-Thomas model (Gent and Thomas, 1958)

$$\boldsymbol{Q}_I(I_1, I_2, I_3) = \underbrace{\left[(I_1 - 3)^m (I_2 - 3)^{n-m} : n \in \{1, \dots, N_{\text{Mooney}}\}, m \in \{0, \dots, n\}\right]^T}_{\text{generalized Mooney–Rivlin features}} \oplus \underbrace{\left[\log\left(I_2/3\right)\right]}_{\text{logarithmic feature}}, \tag{4}$$

where $\oplus$ denotes vector concatenation and the choice of N_{Mooney} dictates the size of the feature vector. This selection of feature functions was proven in Flaschel et al. (2021) to have a high approximation power. We choose $N_{\text{Mooney}} = 3$ in this work, such that $\boldsymbol{\theta}_I$ comprises 10 unknown parameters.

To obtain a general parametric ansatz for the principal stretch dependent contribution $\tilde{W}_\lambda$, we consider the generalized Ogden model (Ogden, 1972)

$$\tilde{W}_\lambda(\lambda_1, \lambda_2, \lambda_3) = \sum_{i=1}^{N_{\text{Ogden}}} \frac{2\mu_i}{\alpha_i^2} \left(\lambda_1^{\alpha_i} + \lambda_2^{\alpha_i} + \lambda_3^{\alpha_i} - 3\right), \tag{5}$$

where μ_i and α_i are unknown real-valued material parameters and N_{Ogden} is the number of considered terms in the generalized Ogden model. In contrast to the model library chosen in Eq. (3), the strain energy density of the generalized Ogden model depends nonlinearly on the unknown material parameters. In general, this complicates the inference of the material parameters from experimental measurements. Therefore, we assume in the following an a priori fixed set of N_{Ogden} distinct candidate values of α_i. By choosing N_{Ogden} sufficiently large, it is expected that this assumption does not significantly restrict the versatility of the model library. In Appendix C, we show numerical evidence that the expressiveness of the model library increases upon increasing N_{Ogden}. We further show in Appendix C that choosing $N_{\text{Ogden}} = 2 \cdot 10^4$ values of α_i evenly distributed between -100 and 100 excluding zero, i.e., $\alpha_i \in \{-100, -99.99, \dots, -0.01, 0.01, \dots, 99.99, 100\}$, provides a sufficiently fine realization of the candidate values of α_i. With this assumption, μ_i remain the only unknowns in the model ansatz for $\tilde{W}_\lambda$ which can now be written as a linear combination of nonlinear feature functions

$$\tilde{W}_\lambda(\lambda_1, \lambda_2, \lambda_3) = \boldsymbol{\theta}_\lambda \cdot \boldsymbol{Q}_\lambda(\lambda_1, \lambda_2, \lambda_3), \tag{6}$$

where the nonlinear feature functions have been collected in the vector $\boldsymbol{Q}_\lambda$ with components

$$\left\{Q_\lambda(\lambda_1, \lambda_2, \lambda_3)\right\}_i = \lambda_1^{\alpha_i} + \lambda_2^{\alpha_i} + \lambda_3^{\alpha_i} - 3, \tag{7}$$

and $\boldsymbol{\theta}_\lambda$ is a vector of unknown real-valued material parameters that are related to the parameters μ_i through $\left\{\theta_\lambda\right\}_i = 2\mu_i/\alpha_i^2$.

By defining

$$\boldsymbol{\theta} = \begin{bmatrix} \boldsymbol{\theta}_I \\ \boldsymbol{\theta}_\lambda \end{bmatrix}, \quad \boldsymbol{Q} = \begin{bmatrix} \boldsymbol{Q}_I(I_1, I_2, I_3) \\ \boldsymbol{Q}_\lambda(\lambda_1, \lambda_2, \lambda_3) \end{bmatrix}, \tag{8}$$

the model library for the strain energy density can be written as

$$W = \boldsymbol{\theta} \cdot \boldsymbol{Q} - p \cdot (J - 1). \tag{9}$$

To ensure that the strain energy density describes physically meaningful material behavior, we assume that $\theta_i \geq 0$ for all i. The non-negativity of the material parameters is a sufficient (but not necessary) requirement for stability, see Hartmann (2001).

2.2. Stress–strain relation

After having defined the strain energy density, a bijective relation between the kinematic state and the stress state of the material is obtained through its differentiation. Specifically, the Piola stress $\mathbf{P}$ is computed by differentiating W with respect to the deformation gradient

$$\mathbf{P} = \frac{\partial W}{\partial \mathbf{F}} = \frac{\partial \tilde{W}}{\partial \mathbf{F}} - p\mathbf{F}^{-T}, \tag{10}$$

where we used $\frac{\partial J}{\partial \mathbf{F}} = J\mathbf{F}^{-T}$. Noting that $\tilde{W} = \boldsymbol{\theta} \cdot \boldsymbol{Q} = \boldsymbol{\theta}_I \cdot \boldsymbol{Q}_I + \boldsymbol{\theta}_\lambda \cdot \boldsymbol{Q}_\lambda$, we apply the chain rule to obtain

$$\frac{\partial \tilde{W}}{\partial F_{ij}} = \boldsymbol{\theta}_I \cdot \left(\frac{\partial \boldsymbol{Q}_I}{\partial I_a} \frac{\partial I_a}{\partial F_{ij}} \right) + \boldsymbol{\theta}_\lambda \cdot \left(\frac{\partial \boldsymbol{Q}_\lambda}{\partial \lambda_b} \frac{\partial \lambda_b}{\partial F_{ij}} \right). \tag{11}$$

The derivatives of the strain invariants and of the principal stretches are provided in Appendices A.1 and A.2, respectively. The derivatives of the feature vectors follow in Appendix A.3. The Cauchy stress $\mathbf{T}$ is calculated from the Piola stress as $\mathbf{T} = \mathbf{P}\mathbf{F}^T$.

2.2.1. Uniaxial compression and tension

Experimental measurements of cylindrical specimens under uniaxial compression and tension deliver labeled data pairs in the form (u_{UT}, F), where u_{UT} is the longitudinal displacement at the displacement controlled end of the specimen and F is the resulting force. Data pairs of the form $(\lambda_{\mathrm{UT}}, P_{11})$, where λ_{UT} is the longitudinal stretch applied to the specimen and P_{11} is the longitudinal normal component of the Piola stress, are obtained through

$$\lambda_{\mathrm{UT}} = \frac{u_{\mathrm{UT}} + h}{h}, \quad P_{11} = \frac{F}{\pi r_{\mathrm{out}}^2}, \tag{12}$$

where h and r_{out} are the height and the outer radius of the undeformed specimen, respectively. The previously introduced material model library can be used to derive a relation $P_{11}(\lambda_{\mathrm{UT}}; \boldsymbol{\theta})$ that links the experimental inputs λ_{UT} and outputs P_{11} depending on the material parameters $\boldsymbol{\theta}$.

Applying a longitudinal stretch λ_{UT} to the specimen implies that $F_{11} = \lambda_{\mathrm{UT}}$ and, due to symmetry, $F_{22} = F_{33}$. As a result of the incompressibility assumption $\det \mathbf{F} \overset{!}{=} 1$, the deformation gradient under uniaxial compression/tension must hence be

$$\mathbf{F}_{\mathrm{UT}} = \begin{bmatrix} \lambda_{\mathrm{UT}} & 0 & 0 \\ 0 & \frac{1}{\sqrt{\lambda_{\mathrm{UT}}}} & 0 \\ 0 & 0 & \frac{1}{\sqrt{\lambda_{\mathrm{UT}}}} \end{bmatrix}. \tag{13}$$

The kinematic state is thus completely determined by the applied longitudinal stretch.

To obtain the relationship $P_{11}(\lambda_{\mathrm{UT}}; \boldsymbol{\theta})$, the unknown hydrostatic pressure p in Eq. (10) needs to be computed. As the material is allowed to freely deform in the x_2- and x_3-directions, it is $P_{22} = P_{33} \overset{!}{=} 0$. This condition is used along with Eq. (10)

$$P_{33} = \frac{\partial \tilde{W}}{\partial F_{33}} - pF_{33}^{-1} \overset{!}{=} 0, \tag{14}$$

to find the hydrostatic pressure

$$p = \frac{\partial \tilde{W}}{\partial F_{33}} F_{33}. \tag{15}$$

We hence obtain the desired relationship by substituting the pressure in Eq. (10)

$$P_{11}(\lambda_{\mathrm{UT}}; \boldsymbol{\theta}) = \frac{\partial \tilde{W}}{\partial F_{11}} - pF_{11}^{-1} = \frac{\partial \tilde{W}}{\partial F_{11}} - \frac{F_{33}}{F_{11}} \frac{\partial \tilde{W}}{\partial F_{33}} = \boldsymbol{\theta} \cdot \underbrace{\left(\frac{\partial \boldsymbol{Q}}{\partial F_{11}} - \frac{F_{33}}{F_{11}} \frac{\partial \boldsymbol{Q}}{\partial F_{33}} \right)}_{\boldsymbol{Q}'_{\mathrm{UT}}(\lambda_{\mathrm{UT}})}, \tag{16}$$

where we denoted all the terms that depend on the longitudinal stretch as $\boldsymbol{Q}'_{\mathrm{UT}}(\lambda_{\mathrm{UT}})$. This can be interpreted as a feature function derivative vector whose scalar product with the material parameters computes the longitudinal normal component of the Piola stress. More information for computing $\boldsymbol{Q}'_{\mathrm{UT}}(\lambda_{\mathrm{UT}})$ is provided in Appendix A.4.

2.2.2. Simple torsion

Now we consider a cylindrical specimen in a cylindrical coordinate system (r, ϑ, z), where r is the radial coordinate, ϑ is the polar angle, and z is the longitudinal coordinate. Assuming the specimen to undergo simple torsion around the z-axis, experimental measurements on specimens under simple torsion deliver labeled data pairs in the form (ϕ, M), where ϕ is the applied angle of deformation at the sheared end of the specimen and M is the resulting torque. The twist ψ of the specimen can be deduced from the applied angle of deformation through $\psi = \phi/h$. The data is transformed into data pairs of the form $(\tilde{\psi}, \tau)$, where $\tilde{\psi} = r_{\text{out}}\psi$ and $\tau = M/r_{\text{out}}^3$ are respectively a normalized twist and normalized torque.

After normalizing the radial coordinate through $\rho = r/r_{\text{out}}$, the deformation gradient in the cylindrical coordinate system then reads (Hartmann, 2001)

$$\mathbf{F}_{\text{ST}} = \begin{bmatrix} F_{rr} & F_{r\vartheta} & F_{rz} \\ F_{\vartheta r} & F_{\vartheta\vartheta} & F_{\vartheta z} \\ F_{zr} & F_{z\vartheta} & F_{zz} \end{bmatrix} = \begin{bmatrix} 1 & 0 & 0 \\ 0 & 1 & \rho\tilde{\psi} \\ 0 & 0 & 1 \end{bmatrix}, \tag{17}$$

The material model library can be used to derive a relation $\tau(\tilde{\psi}; \boldsymbol{\theta})$ that links the experimental inputs $\tilde{\psi}$ and outputs τ depending on the material parameters $\boldsymbol{\theta}$.

The normalized torque is given by

$$\tau = \int_0^1 2\pi\rho^2 T_{\vartheta z} \, \mathrm{d}\rho, \tag{18}$$

where the component of the Cauchy stress $T_{\vartheta z}$ is, due to Eq. (17),

$$T_{\vartheta z} = P_{\vartheta i} F_{zi} = P_{\vartheta z}. \tag{19}$$

With reference to Eq. (10), we notice that there is no hydrostatic pressure contribution to $P_{\vartheta z}$ under simple torsion, such that

$$T_{\vartheta z} = \frac{\partial W}{\partial F_{\vartheta z}} = \frac{\partial \tilde{W}}{\partial F_{\vartheta z}} = \boldsymbol{\theta} \cdot \frac{\partial \boldsymbol{Q}}{\partial F_{\vartheta z}}. \tag{20}$$

We finally obtain the desired relationship $\tau(\tilde{\psi}; \boldsymbol{\theta})$ by substituting Eq. (20) in Eq. (18)

$$\tau(\tilde{\psi}; \boldsymbol{\theta}) = \boldsymbol{\theta} \cdot \underbrace{\int_0^1 2\pi\rho^2 \frac{\partial \boldsymbol{Q}}{\partial F_{\vartheta z}} \, \mathrm{d}\rho}_{\boldsymbol{Q}'_{\text{ST}}(\tilde{\psi})}, \tag{21}$$

where we denoted all the terms that depend on the twist as $\boldsymbol{Q}'_{\text{ST}}(\tilde{\psi})$. This can be interpreted as a feature function derivative vector whose scalar product with the material parameters computes the normalized torque. More information for computing $\boldsymbol{Q}'_{\text{ST}}(\tilde{\psi})$ is provided in Appendix A.5.

3. Model discovery

After having defined the material model library, i.e., a versatile ansatz for the hyperelastic strain energy density, we seek an optimal choice of the material model parameters $\boldsymbol{\theta}$. Specifically, in the spirit of EUCLID — see Flaschel et al. (2021) — we seek a parameter vector $\boldsymbol{\theta}$ which leads at the same time to a small mismatch between the material model predictions and the experimental measurements, and to a simple discovered material model, i.e., one with a small number of terms. Unlike in the original work on EUCLID (Flaschel et al., 2021), in which the model selection was driven by a physics-informed optimization problem that was fed by unlabeled data, in this paper, labeled data pairs (i.e., stress versus strain data pairs under uniaxial compression/tension, and twist versus torque data pairs under simple torsion) are available to drive the model selection. Thus, the method proposed here can be interpreted as a supervised counterpart to the originally proposed EUCLID. The proposed algorithm for inferring $\boldsymbol{\theta}$ is described in the following and a step-by-step overview is provided in Appendix B, see Fig. B.10.

3.1. Model-data mismatch

First, a quantitative measure of the mismatch between the material model predictions and the experimental measurements needs to be introduced. In the case of uniaxial compression/tension, the measurements are provided in the form of pairs $(\lambda_{\text{UT}}^{(l)}, P_{11}^{(l)})$ for a number of load steps $l = 1, \dots, n_{\text{UT}}$. Eq. (16) provides a mapping between the input and output data, thus leading to n_{UT} equations

$$P_{11}(\lambda_{\text{UT}}^{(l)}; \boldsymbol{\theta}) = P_{11}^{(l)}. \tag{22}$$

Noting that each of the equations above depends linearly on $\boldsymbol{\theta}$, we write them as a linear system of equations

$$\mathbf{A}_{\text{UT}}\boldsymbol{\theta} = \boldsymbol{b}_{\text{UT}}, \tag{23}$$

with

$$\mathbf{A}_{\text{UT}} = \begin{bmatrix} \left(\boldsymbol{Q}'_{\text{UT}}(\lambda_{\text{UT}}^{(1)})\right)^T \\ \vdots \\ \left(\boldsymbol{Q}'_{\text{UT}}(\lambda_{\text{UT}}^{(n_{\text{UT}})})\right)^T \end{bmatrix}, \quad \boldsymbol{b}_{\text{UT}} = \begin{bmatrix} P_{11}^{(1)} \\ \vdots \\ P_{11}^{(n_{\text{UT}})} \end{bmatrix}. \tag{24}$$

Analogously, in the case of simple torsion, the measurements are provided in the form of pairs $(\tilde{\psi}^{(l)}, \tau^{(l)})$ for a number of load steps $l = 1, \dots, n_{\mathrm{ST}}$. Eq. (21) provides a mapping between the input and output data, thus leading to n_{ST} equations

$$\tau(\tilde{\psi}^{(l)}; \boldsymbol{\theta}) = \tau^{(l)}. \tag{25}$$

which can be expressed once again as a linear system of equations

$$\mathbf{A}_{\mathrm{ST}}\boldsymbol{\theta} = \boldsymbol{b}_{\mathrm{ST}}, \tag{26}$$

with

$$\mathbf{A}_{\mathrm{ST}} = \begin{bmatrix} \left(\boldsymbol{Q}'_{\mathrm{ST}}(\tilde{\psi}^{(1)})\right)^T \\ \vdots \\ \left(\boldsymbol{Q}'_{\mathrm{ST}}(\tilde{\psi}^{(n_{\mathrm{ST}})})\right)^T \end{bmatrix}, \quad \boldsymbol{b}_{\mathrm{ST}} = \begin{bmatrix} \tau^{(1)} \\ \vdots \\ \tau^{(n_{\mathrm{ST}})} \end{bmatrix}. \tag{27}$$

The linear systems in Eqs. (23) and (26) are concatenated to the system $\mathbf{A}\boldsymbol{\theta} = \boldsymbol{b}$ with

$$\mathbf{A} = \begin{bmatrix} r_{\mathrm{UT}}\mathbf{A}_{\mathrm{UT}} \\ r_{\mathrm{ST}}\mathbf{A}_{\mathrm{ST}} \end{bmatrix}, \quad \boldsymbol{b} = \begin{bmatrix} r_{\mathrm{UT}}\boldsymbol{b}_{\mathrm{UT}} \\ r_{\mathrm{ST}}\boldsymbol{b}_{\mathrm{ST}} \end{bmatrix}, \tag{28}$$

where $r_{\mathrm{UT}} > 0$ and $r_{\mathrm{ST}} > 0$ scale the contributions of the uniaxial compression/tension data and the simple torsion data, respectively. During the experimental investigations conducted in the context of this work (see, e.g., Section 5), the chosen range of applied deformation in uniaxial compression/tension and simple torsion led to measurements $\boldsymbol{b}_{\mathrm{UT}}$ and $\boldsymbol{b}_{\mathrm{ST}}$, respectively, that were different in magnitude. Choosing $r_{\mathrm{UT}} = 0.3$ and $r_{\mathrm{ST}} = 1$ was found to result in a proper scaling of the contributions from uniaxial compression/tension and simple torsion, leading to similar maximum absolute entries in the scaled measurements $r_{\mathrm{UT}}\boldsymbol{b}_{\mathrm{UT}}$ and $r_{\mathrm{ST}}\boldsymbol{b}_{\mathrm{ST}}$. Finally, the total mismatch between the material model prediction and the experimental measurements is quantified by computing the mean squared error MSE of the residuals of the linear system of equations

$$\mathrm{MSE}(\boldsymbol{\theta}) = \frac{1}{n_{\mathrm{UT}} + n_{\mathrm{ST}}} \|\mathbf{A}\boldsymbol{\theta} - \boldsymbol{b}\|_2^2. \tag{29}$$

3.2. Feature scaling

To obtain a system of equations with dimensionless parameters and system coefficients, we standardize the system of equations. Defining the mean and standard deviation of a vector $\boldsymbol{x} \in \mathbb{R}^n$ as

$$\mathrm{Mean}(\boldsymbol{x}) = \frac{1}{n}\sum_i x_i, \quad \mathrm{Std}(\boldsymbol{x}) = \sqrt{\frac{1}{n}\sum_i \left(x_i - \mathrm{Mean}(\boldsymbol{x})\right)^2}, \tag{30}$$

the standardized system of equations reads

$$\bar{\mathbf{A}}\bar{\boldsymbol{\theta}} = \bar{\boldsymbol{b}} \tag{31}$$

with

$$\bar{A}_{ij} = \frac{A_{ij}}{\mathrm{Std}(\boldsymbol{A}_j)}, \quad \bar{b}_i = \frac{b_i}{\mathrm{Std}(\boldsymbol{b})}, \quad \bar{\theta}_j = \frac{\mathrm{Std}(\boldsymbol{A}_j)}{\mathrm{Std}(\boldsymbol{b})}\theta_j, \tag{32}$$

where we defined $\boldsymbol{A}_j$ as the jth column of $\mathbf{A}$. The mean squared error of the residuals of the standardized linear system of equations is defined as

$$\overline{\mathrm{MSE}}(\bar{\boldsymbol{\theta}}) = \frac{1}{n_{\mathrm{UT}} + n_{\mathrm{ST}}} \|\bar{\mathbf{A}}\bar{\boldsymbol{\theta}} - \bar{\boldsymbol{b}}\|_2^2. \tag{33}$$

3.3. Optimization problem

Our objectives are to calibrate the unknown material parameters such that the material model is in agreement with the experimental data, and to discard those terms in the model ansatz which have a minor influence on the fitting accuracy by setting their corresponding parameters to zero. To this end, we solve an L_1-regularized optimization problem (also denoted as sparse regression problem) of the form

$$\bar{\boldsymbol{\theta}}^{\mathrm{opt}} = \underset{\bar{\boldsymbol{\theta}} \geq \mathbf{0}}{\arg\min} \left(\frac{1}{2}\overline{\mathrm{MSE}}(\bar{\boldsymbol{\theta}}) + \lambda_p \|\bar{\boldsymbol{\theta}}\|_1 \right), \tag{34}$$

where $\overline{\mathrm{MSE}}(\bar{\boldsymbol{\theta}})$ is the previously introduced mean squared error function that quantifies the mismatch between the material model predictions and the experimental data, and $\|\bar{\boldsymbol{\theta}}\|_1 = \sum_i |\bar{\theta}_i|$ is an L_1-regularization term, also denoted as *Lasso* (least absolute shrinkage and selection operator). This term was first used for model selection by Frank and Friedman (1993) and Tibshirani (1996) and later applied to problems in dynamics by Brunton et al. (2016). It can be interpreted as a convex and continuous approximation of the non-convex and non-continuous operator that counts the number of nonzero entries in the material parameter vector (usually denoted as $\|\bar{\boldsymbol{\theta}}\|_0$). Thus, adding the L_1-regularization term to the minimization problem promotes sparsity of the material parameter vector. In previous works (Flaschel et al., 2021, 2022), the more general L_p-regularization term $\|\bar{\boldsymbol{\theta}}\|_p^p = \sum_i |\bar{\theta}_i|^p$ with $0 < p \leq 1$ was

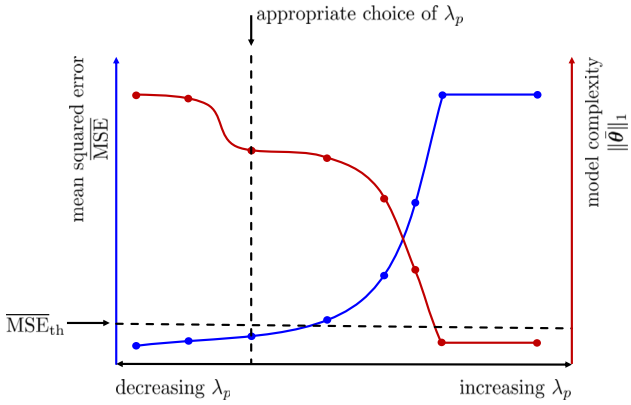

Fig. 1. Qualitative illustration of the Pareto analysis for selecting an appropriate value of λ_p.

adopted to promote sparsity in the solution vector. The L_p term has the advantage that it converges to the operator that counts the number of nonzero entries in the material parameter vector as p approaches zero. Thus, it can be considered as a better measure of sparsity than the L_1-regularization term. However, the L_p term is non-convex for $p < 1$; this implies that the optimization problem becomes non-convex and thus multiple solutions are to be expected, corresponding to local minima of the objective function. In our previous papers (Flaschel et al., 2021, 2022), this issue was addressed by solving the optimization problem multiple times and selecting the minimum of the computed local minima, which obviously increases the computational complexity and cost of the minimization problem. In this work, we rely on the L_1-regularization term and thus solve a convex minimization problem which thus admits a unique solution. The influence of the regularization is governed by the choice of the weighting factor $\lambda_p \geq 0$. As proposed in Flaschel et al. (2022, 2023) and Marino et al. (2023), an appropriate choice of λ_p for striking a balance between fitting accuracy and mathematical complexity of the material model is obtained through a Pareto analysis (see Section 3.5).

3.4. Solver

To solve the problem in Eq. (34), we leverage a coordinate descent algorithm as proposed by Friedman et al. (2010). In comparison to the fixed-point iteration used in our previous work on hyperelastic material model discovery (Flaschel et al., 2021) in which a nonconvex optimization problem was solved, the coordinate descent algorithm is computationally more efficient as it makes use of the fact that the L_1-regularized problem is convex. The coordinate descent algorithm is implemented in the *Lasso* subroutine of the open-source Python library *sklearn*. The subroutine takes $\bar{\mathbf{A}}$ and $\bar{\boldsymbol{b}}$ as well as the value of λ_p as input and returns the sparse solution vector $\bar{\boldsymbol{\theta}}$ (for each value of λ_p) whose entries are constrained to be greater than or equal to zero. The intercept in the *Lasso* subroutine is turned off and the maximum number of iterations is set to 10^4.

3.5. Pareto analysis

The solution of the problem in Eq. (34) is highly dependent on the choice of λ_p. As qualitatively illustrated in Fig. 1, a small value of λ_p yields a dense solution vector and therefore a complex expression for the material model that is in general associated with a high fitting accuracy, i.e., a small mean squared error. Increasing the value of λ_p results in a sparser solution vector and thus a simpler expression for the material model at the cost of a reduced fitting accuracy with a larger mean squared error. In the limit of very large values of λ_p, the optimization problem returns a solution vector with only zero entries and the mean squared error saturates.

To strike a balance between the accuracy and the complexity of the material model, a Pareto analysis is applied to the problem. To this end, the problem in Eq. (34) is solved multiple times using a set of different λ_p values, leading to a solution vector $\bar{\boldsymbol{\theta}}$ for every choice of λ_p. Here, we choose 41 values of λ_p that are evenly distributed on a logarithmic scale between 10^{-2} and 10^2. Our objective now is to select from all solutions the one that exhibits an optimal combination of high fitting accuracy and high sparsity. To this end, the mean squared error and the L_1-norm of the solution vector are computed for each solution. The minimum and maximum mean squared errors among all solutions are denoted as $\overline{\text{MSE}}_{\text{min}}$ and $\overline{\text{MSE}}_{\text{max}}$, respectively. Further, we define a threshold mean squared error (see Fig. 1) as

$$\overline{\text{MSE}}_{\text{th}} = \overline{\text{MSE}}_{\text{min}} + r_\lambda(\overline{\text{MSE}}_{\text{max}} - \overline{\text{MSE}}_{\text{min}}), \tag{35}$$

where r_λ is a small positive scalar, $0 < r_\lambda \ll 1$. All solutions for which the mean squared errors are greater than this threshold are expected to exhibit a low fitting accuracy and are thus discarded. From the remaining solutions, i.e., those for which the mean squared error is below $\overline{\text{MSE}}_{\text{th}}$, we select the sparsest one, i.e., the solution with the lowest value of the L_1-norm term (see Fig. 1). In this way, a sparse solution with a low mean squared error is obtained, whereby the amount of sparsity is dictated by the user-defined hyperparameter r_λ. In this work we set $r_\lambda = 0.02$ and keep it constant throughout the analyses.

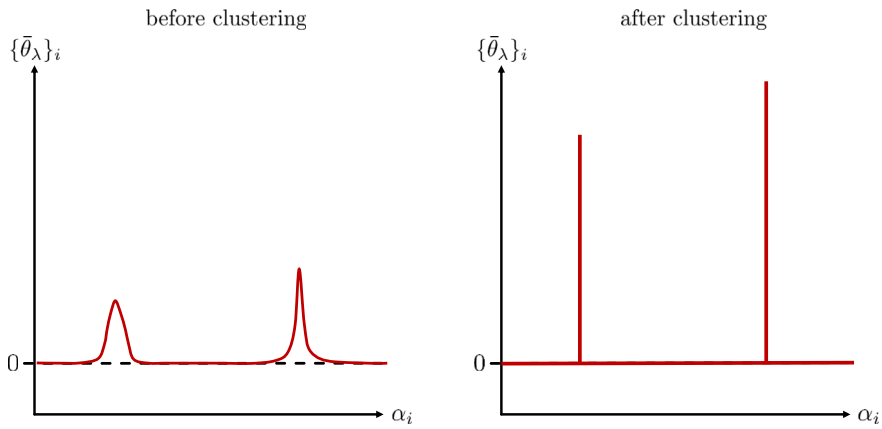

Fig. 2. Qualitative illustration of the feature clustering.

3.6. Thresholding

The solution vector $\bar{\boldsymbol{\theta}}$ selected in Section 3.5 may contain values that are close to zero. As these material parameters and their corresponding features have a vanishing effect on the model response, they are set to zero. Specifically, we define a threshold value $\bar{\theta}_{\text{th}}$ (here chosen as $\bar{\theta}_{\text{th}} = 0.01$) and we set $\bar{\theta}_i = 0$ if $\bar{\theta}_i < \bar{\theta}_{\text{th}}$ for all i.

3.7. Feature clustering

Due to the fine discretization of the chosen range of α_i values (see Section 2), the feature library contains Ogden features with very similar values of α_i, which in turn results in a high correlation between these features. While the solution vector obtained by solving the optimization problem with *Lasso* regularization already exhibits a high degree of sparsity, the sparsity and thus interpretability of the material model can be further improved by grouping together highly correlated features in the solution. To this end, we leverage a clustering algorithm that automatically groups together similar α_i values, as qualitatively illustrated in Fig. 2. For a similar clustering strategy that was used to group together similar Maxwell elements in viscoelastic constitutive laws discovered with EUCLID, the interested reader is referred to Marino et al. (2023).

In this paper, we adopt the clustering method *DBSCAN* (Density-Based Spatial Clustering of Applications with Noise) (Ester et al., 1996) as implemented in the Python library *sklearn*. *DBSCAN* assigns each α_i whose corresponding $\{\bar{\theta}_\lambda\}_i$ is non-zero to a cluster. This is done in such a way that for each α_i in a cluster there exists at least one value α_j (with $i \neq j$) in the same cluster such that their distance $|\alpha_i - \alpha_j|$ is smaller than or equal to a predefined value, here chosen as 0.01. The advantage over the k-means clustering algorithm used in Marino et al. (2023) is that the needed number of clusters is obtained automatically. After grouping the α_i values into a set of clusters, an averaged value $\bar{\alpha}$ is computed for each cluster as

$$\bar{\alpha} = \frac{\sum_k \alpha_k \{\bar{\theta}_\lambda\}_k}{\sum_k \{\bar{\theta}_\lambda\}_k}, \tag{36}$$

where k ranges over all elements in the considered cluster. Afterwards, $\bar{\alpha}$ is rounded to the closest original value of α_i contained in the material model library (see Section 2). Thus, we identify for each cluster one value of α_i for which the corresponding coefficient in $\bar{\boldsymbol{\theta}}_\lambda$ is non-zero, while all other entries in $\bar{\boldsymbol{\theta}}_\lambda$ are set to zero.

3.8. Final regression without regularization

By solving the sparse regression problem and applying the clustering method, a small number of relevant features are automatically selected from the originally large library of candidate features. In a final step, all features corresponding to parameters that have been identified as zero are disregarded from the library by removing the corresponding columns from the matrix $\bar{\mathbf{A}}$, thus obtaining a reduced system matrix $\bar{\mathbf{A}}_{\text{red}}$. Afterwards, the reduced regression problem is solved for the remaining non-zero parameters $\bar{\boldsymbol{\theta}}_{\text{red}}$, but this time without introducing any regularization term (i.e., we solve Eq. (34) with $\lambda_p = 0$).

The motivation behind this last step is twofold. First, while the regularization term in Eq. (34) forces unneeded parameters to zero, it simultaneously shrinks the absolute value of the relevant parameters. Solving the regression problem without regularization for the small number of selected features leads to material parameters that are not affected by such shrinkage. And second, after applying the clustering method, most entries in $\bar{\boldsymbol{\theta}}_\lambda$ have been identified as zero, while the remaining non-zero parameters in $\bar{\boldsymbol{\theta}}_\lambda$ are still unknown. The final regression problem without regularization is used to calibrate those non-zero parameters. Finally, the original parameters $\boldsymbol{\theta}$ can be recovered from the scaled parameters $\bar{\boldsymbol{\theta}}$ using Eq. (32).

Table 1
Strain energy density functions of the true and discovered material models and MSE of predictions.

Benchmarks		Strain energy density $\tilde{W}$ [Pa]	MSE [Pa^2]	$\overline{\text{MSE}}$ [−]
MR1	Truth	$40.00\left(I_1-3\right) + 20.00\left(I_2-3\right)$	–	–
	$\sigma=0$	$40.00\left(I_1-3\right) + 20.00\left(I_2-3\right)$	0.0000	0.0000
	$\sigma=5$ Pa	$41.25\left(I_1-3\right) + 17.71\left(I_2-3\right)$	13.4120	0.0022
	$\sigma=10$ Pa	$42.51\left(I_1-3\right) + 15.42\left(I_2-3\right)$	53.6481	0.0090
O1	Truth	$2.00\left(\lambda_1^{-10.00}+\lambda_2^{-10.00}+\lambda_3^{-10.00}-3\right)$	–	–
	$\sigma=0$	$1.97\left(\lambda_1^{-10.03}+\lambda_2^{-10.03}+\lambda_3^{-10.03}-3\right)$	0.1815	0.0000
	$\sigma=5$ Pa	$1.94\left(\lambda_1^{-10.05}+\lambda_2^{-10.05}+\lambda_3^{-10.05}-3\right)$	13.5305	0.0001
	$\sigma=10$ Pa	$1.91\left(\lambda_1^{-10.08}+\lambda_2^{-10.08}+\lambda_3^{-10.08}-3\right)$	53.8606	0.0006
O2	Truth	$16.00\left(\lambda_1^{-5.00}+\lambda_2^{-5.00}+\lambda_3^{-5.00}-3\right) + 8.00\left(\lambda_1^{5.00}+\lambda_2^{5.00}+\lambda_3^{5.00}-3\right)$	–	–
	$\sigma=0$	$13.50\left(\lambda_1^{-5.25}+\lambda_2^{-5.25}+\lambda_3^{-5.25}-3\right) + 11.79\left(\lambda_1^{4.43}+\lambda_2^{4.43}+\lambda_3^{4.43}-3\right)$	0.2936	0.0000
	$\sigma=5$ Pa	$13.29\left(\lambda_1^{-5.26}+\lambda_2^{-5.26}+\lambda_3^{-5.26}-3\right) + 11.79\left(\lambda_1^{4.44}+\lambda_2^{4.44}+\lambda_3^{4.44}-3\right)$	13.7349	0.0002
	$\sigma=10$ Pa	$13.16\left(\lambda_1^{-5.26}+\lambda_2^{-5.26}+\lambda_3^{-5.26}-3\right) + 11.75\left(\lambda_1^{4.45}+\lambda_2^{4.45}+\lambda_3^{4.45}-3\right)$	54.0784	0.0007
MR2O1	Truth	$30.00\left(I_2-3\right)^2 + 2.00\left(\lambda_1^{-10.00}+\lambda_2^{-10.00}+\lambda_3^{-10.00}-3\right)$	–	–
	$\sigma=0$	$29.25\left(I_2-3\right)^2 + 1.97\left(\lambda_1^{-10.04}+\lambda_2^{-10.04}+\lambda_3^{-10.04}-3\right)$	0.3179	0.0000
	$\sigma=5$ Pa	$31.69\left(I_2-3\right)^2 + 1.91\left(\lambda_1^{-10.07}+\lambda_2^{-10.07}+\lambda_3^{-10.07}-3\right)$	13.7564	0.0002
	$\sigma=10$ Pa	$34.16\left(I_2-3\right)^2 + 1.86\left(\lambda_1^{-10.10}+\lambda_2^{-10.10}+\lambda_3^{-10.10}-3\right)$	53.9747	0.0007

4. Numerical verification

4.1. Synthetical data

Before applying the proposed method for material model discovery to experimental data, we verify the method on synthetically generated data without and with artificially added noise. Such data are obtained by assuming different hyperelastic material models and generating labeled data pairs under the assumption of uniaxial compression/tension and simple torsion. Specifically, we consider the four material models whose strain energy density functions are provided in Table 1:

- first-order Mooney–Rivlin model (MR1)
- one-term Ogden model (O1)
- two-term Ogden model (O2)
- combination of second-order Mooney–Rivlin model and one-term Ogden model (MR2O1)

The chosen material models are used to generate $n_{\text{UT}} = 60$ pairs of data for uniaxial compression/tension, i.e., $(\lambda_{\text{UT}}^{(l)}, P_{11}^{(l)})$, where the values of $\lambda_{\text{UT}}^{(l)}$ are equally spaced between $\lambda_{\text{UT}}^{(1)} = 0.7$ and $\lambda_{\text{UT}}^{(n_{\text{UT}})} = 1.3$, and $n_{\text{ST}} = 60$ pairs of data for simple torsion, i.e., $(\tilde{\psi}^{(l)}, \tau^{(l)})$, where the values of $\tilde{\psi}^{(l)}$ are equally spaced between $\tilde{\psi}^{(1)} = -1$ and $\tilde{\psi}^{(n_{\text{ST}})} = 1$.

To emulate real experimental data, the generated data are perturbed by artificial noise by considering noisy data pairs $(\lambda_{\text{UT}}^{(l)}, P_{11}^{(l)} + \varepsilon_{\text{UT}}^{(l)})$ and $(\tilde{\psi}^{(l)}, \tau^{(l)} + \varepsilon_{\text{ST}}^{(l)})$, where $\varepsilon_{\text{UT}}^{(l)} \sim \mathcal{N}\left(0, \sigma^2\right)$ and $\varepsilon_{\text{ST}}^{(l)} \sim \mathcal{N}\left(0, \sigma^2\right)$ is random noise that is drawn independently from a Gaussian distribution with zero mean and standard deviation σ. Here, we consider (beside the noiseless case) two different levels of noise, i.e., $\sigma \in \{0\text{ Pa}, 5\text{ Pa}, 10\text{ Pa}\}$.

4.2. Results and discussion

The synthetically generated data serve as input for the proposed algorithm for material model discovery. Testing the method on synthetical data has the advantage that the discovered material models can be compared to the "ground truth" (in machine learning jargon), i.e., to the material models that were assumed during data generation. Table 1 shows the expressions of the discovered strain energy density functions in comparison with the true ones. It is observed that the correct mathematical form of the strain energy density function is recovered for each test case. Table 1 further provides the mean squared errors that quantify the mismatch between the data and the predictions of the discovered models. As expected, the MSE increases for increasing level of noise.

For the benchmark case MR1, the material coefficients in the strain energy density function are exactly recovered for the noiseless case. The deviation between the true and identified parameters increases for increasing noise, as expected. For the benchmark cases O1 and MR2O1, the true and discovered parameters are in excellent agreement. However, the material parameters are not exactly recovered even in the noiseless case. The reason for this is that computing the averaged values $\bar{\alpha}$ after the feature clustering (Section 3.7) cannot exactly recover the ground truth exponents in the Ogden terms, which leads to small deviations in the identified parameters. For the benchmark case O2, the true and identified parameters exhibit slightly larger deviations. One explanation for these deviations could be that the model library comprises many material models and many combinations of material parameters

that are equally suited to describe the material response. The proposed algorithm does not guarantee to find exactly the same model and parameters that were assumed during data generation, but may instead provide an adequate surrogate model that is equally suited to predict the data. We emphasize that, although the true and identified material parameters show some deviations, the MSE for the benchmark case O2 is similar to the MSE for the other benchmarks. Thus, the deviation in the model parameters does not seem to seriously affect the fitting accuracy of the model.

Fig. 3 illustrates the material response of the discovered material models in direct comparison with the synthetically generated data for the case with the highest level of noise, revealing an excellent agreement.

In the following, we discuss in more detail some of the intermediate steps in the sparsity promoting algorithm for material model discovery (see Steps 3–8 in Fig. B.10) in the context of benchmark case MR2O1 with noise level $\sigma = 10$ Pa. Fig. 4 illustrates the Pareto analysis, which is leveraged for the choice of the hyperparameter λ_p in the sparse regression problem. It can be seen that the mean squared error $\overline{\text{MSE}}$ increases and the L_1-norm of the material parameter vector $\|\bar{\theta}\|_1$ decreases for increasing values of λ_p. For values of λ_p exceeding approximately 1, the material parameter vector obtained from the solution of the sparse regression problem contains all zeros, so that its L_1-norm remains constant at zero and the corresponding $\overline{\text{MSE}}$ saturates. Using the method described in Section 3.5, the appropriate value of λ_p is chosen such that the selected model exhibits both a high fitting accuracy and a low model complexity. Note also that for values of λ_p lower than the chosen one, the $\overline{\text{MSE}}$ is very weakly sensitive to the specific choice of λ_p.

In Fig. 5, the effect of the clustering algorithm (see Section 3.7) is illustrated. Before applying the clustering method, many values of α_i are zero while some non-zero values agglomerate in a small region near the ground truth value (equal to 10, see Table 1). The clustering algorithm identifies these values as one cluster. Afterwards, the values of α_i belonging to the cluster are averaged, such that the discovered material model exhibits only one Ogden term as the ground truth model, and the feature coefficients are calibrated, as illustrated in Section 3.8.

5. Experimental validation

5.1. Experimental data

In the context of this work, we use multi-modal large-strain mechanical testing data from 81 cylindrical specimens extracted from three different human brains. The data acquisition and preprocessing are briefly described in the following. For details, the reader is referred to Hinrichsen et al. (2022).

81 cylindrical specimens from different regions of the brain are prepared. Each specimen is labeled by a brain number and a specimen number as HBE_⟨brain no.⟩_⟨specimen no.⟩. The specimens have a radius of approximately $r_{\text{out}} \approx 4$ mm. The heights of the specimens and the region that they stem from are recorded in Table D.3.

Fig. 6 shows one of the human brains and an exemplary cylindrical sample before and after mounting it to the rheometer for the mechanical testing. Each loading mode (compression/tension and torsional shear) consists of three cycles. Here, we use the data from the third cycle representing the preconditioned material response as brain tissue was found to show substantial pre-conditioning behavior (Budday et al., 2017). We limit ourselves to hyperelastic material models (neglecting poro- and viscoelastic effects). The strain rates needed to obtain a purely hyperelastic response are (in theory infinitely) high or low and therefore not feasible in actual experiments. Thus, the experimental data obtained from the rheometer shows a considerable hysteresis (see Fig. 6) and we extract the hyperelastic response through a preprocessing procedure. First, a moving average as well as a low pass filter is applied to reduce high frequency noises. Afterwards, the hyperelastic response is approximated by the averaged loading and unloading curves (see also Budday et al., 2017). The raw data and the extracted hyperelastic response are illustrated in Fig. 6. To reduce the dimensionality of the data while still preserving the characteristic shape of the curve, we reduce the points per deformation mode to 60.

This finally leads to a number of $n_{\text{UT}} = 60$ data pairs $(\lambda_{\text{UT}}^{(l)}, P_{11}^{(l)})$ and $n_{\text{ST}} = 60$ data pairs $(\tilde{\psi}^{(l)}, \tau^{(l)})$ acquired from the mechanical tests under uniaxial compression/tension and simple torsion, respectively. The values of $\lambda_{\text{UT}}^{(l)}$ are uniformly distributed between $\lambda_{\text{UT}}^{(1)} = 0.85$ and $\lambda_{\text{UT}}^{(n_{\text{UT}})} = 1.15$ and the values of $\tilde{\psi}^{(l)}$ are uniformly distributed between $\tilde{\psi}^{(1)} = -0.3$ and $\tilde{\psi}^{(n_{\text{ST}})} = 0.3$.

5.2. Results and discussion

The proposed algorithm for material model discovery is applied to all experimentally acquired data sets, keeping all hyperparameters and algorithmic settings constant. The resulting material parameters are listed in Tables E.5 and E.6. Many material parameters are identified as zero, meaning that the discovered expressions of the strain energy density functions are concise and interpretable. The material model discovered for most of the specimens (i.e., about 60% of the specimens) is the one-term Ogden model, which has also previously been used to fit human brain tissue data (Budday et al., 2017, 2020; Hinrichsen et al., 2022). Further models that were identified are the two-term Ogden model (about 32% of the specimens), and combinations of the one-term Ogden model with a Mooney–Rivlin term (about 7% of the specimens).

To measure the ability of the discovered material models to fit the given experimental data, the mean squared errors MSE and $\overline{\text{MSE}}$ are provided in Tables E.5 and E.6. The scaled mean squared error $\overline{\text{MSE}}$ ranges from a minimum value of 0.01 to a maximum value of 0.71, and the average $\overline{\text{MSE}}$ over all experimental data sets is 0.17.

Fig. 7 shows the stress versus stretch response under uniaxial compression/tension and torque versus normalized twist response under simple torsion of a discovered material model for which the value of $\overline{\text{MSE}}$ is small in comparison to the other experiments.

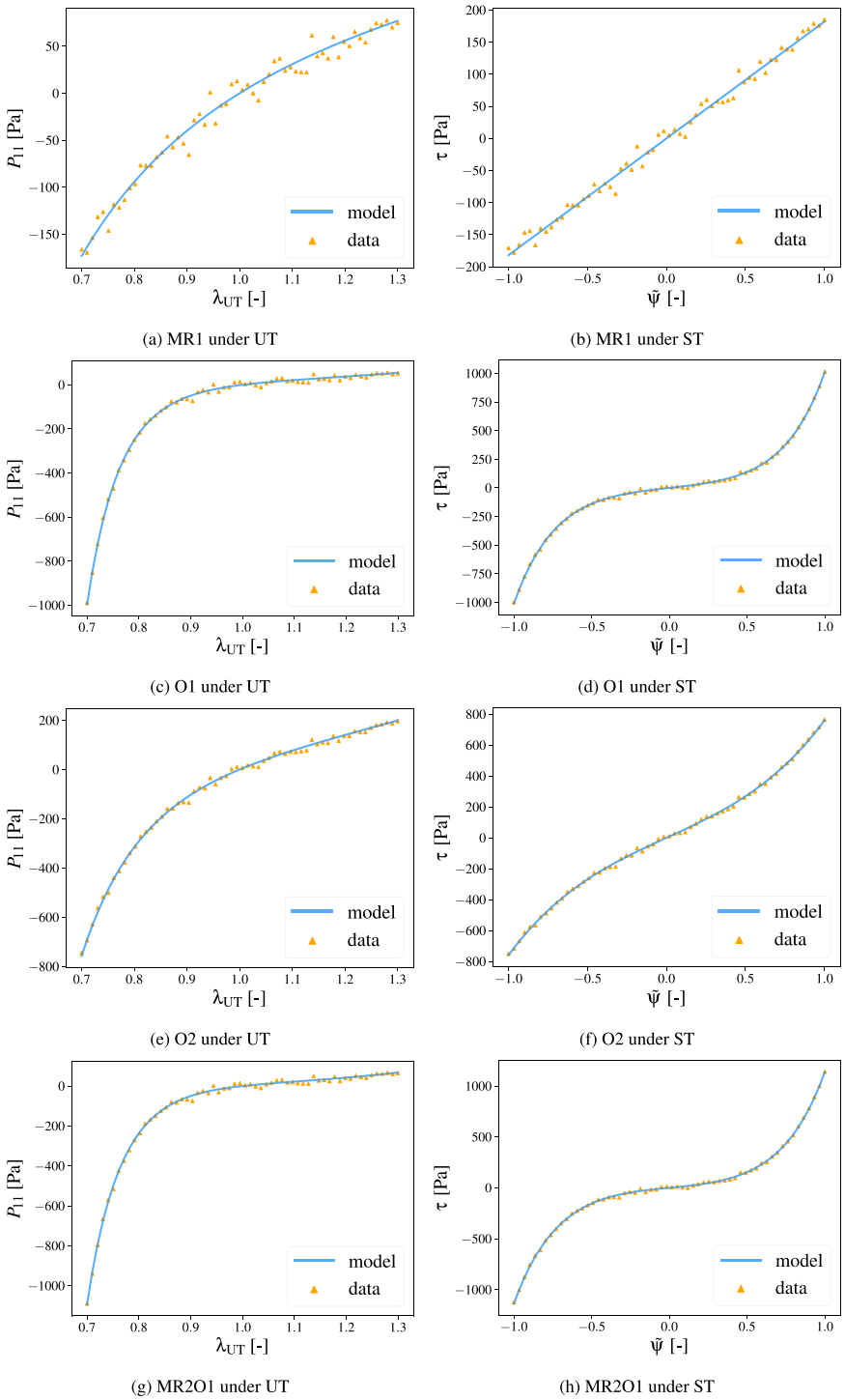

(a) MR1 under UT
(b) MR1 under ST
(c) O1 under UT
(d) O1 under ST
(e) O2 under UT
(f) O2 under ST
(g) MR2O1 under UT
(h) MR2O1 under ST

Fig. 3. Stretch versus stress response under uniaxial compression/tension and (normalized) twist versus torque response under simple torsion of the discovered material models in comparison with the synthetical data (noise level $\sigma = 10$ Pa).

It is evident that the discovered material model is very well suited to describe the given data. Fig. 8 shows the same plots for discovered material models for which the values of $\overline{\text{MSE}}$ are close to the average value of $\overline{\text{MSE}}$ over all experiments. The models are in qualitative agreement with the data. However, especially for the response under uniaxial compression/tension, the models are not capable to precisely match the given data. These deviations could possibly be attributed to modeling assumptions that do not hold

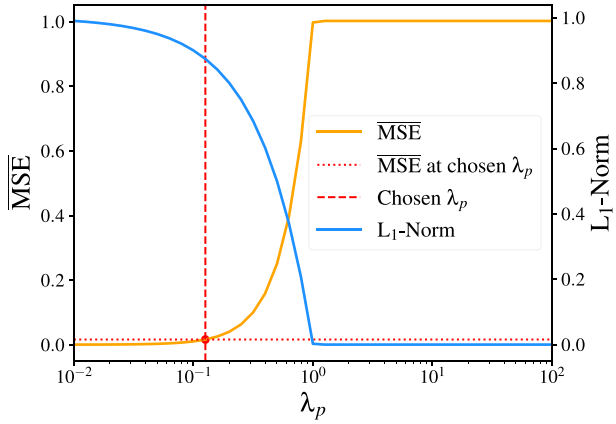

Fig. 4. Illustration of the Pareto analysis for benchmark case MR2O1 (noise level $\sigma = 10$ Pa).

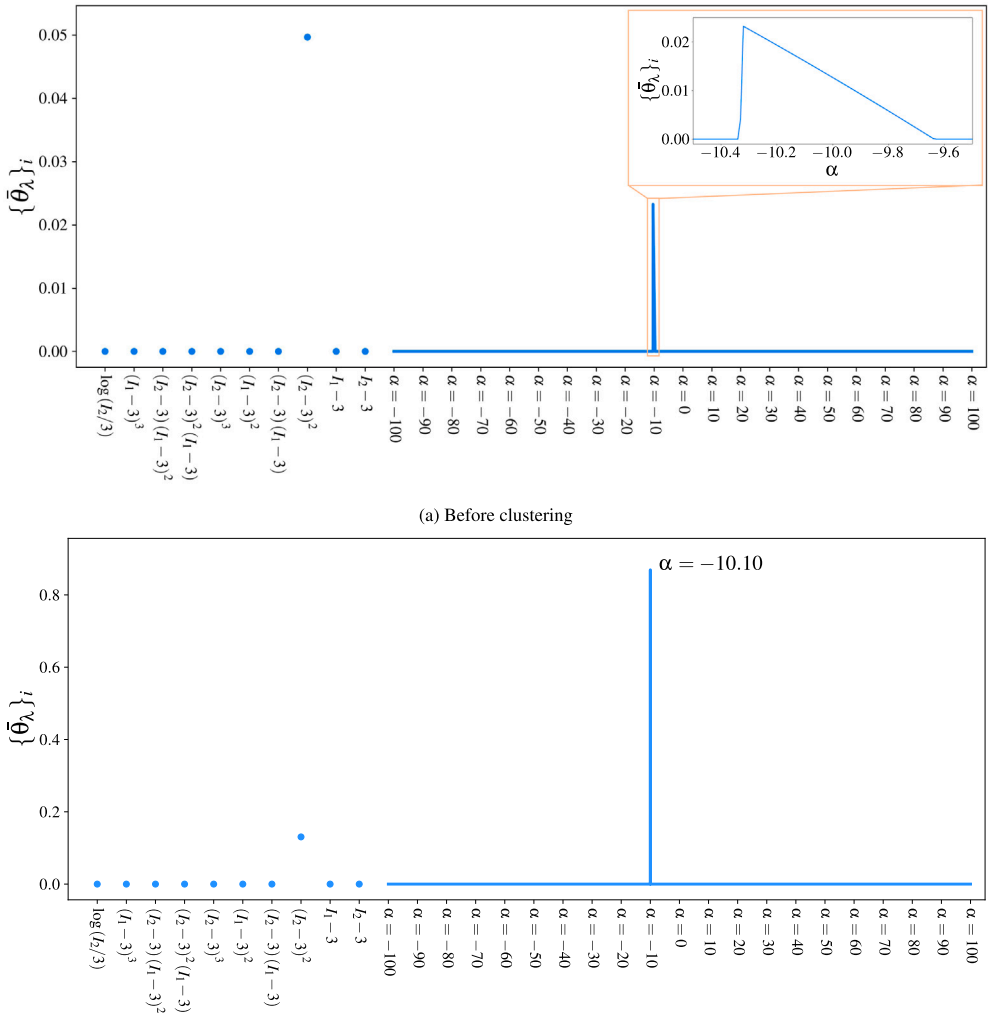

(a) Before clustering

(b) After clustering and final regression without regularization

Fig. 5. Illustration of the feature clustering for benchmark case MR2O1 (noise level $\sigma = 10$ Pa).

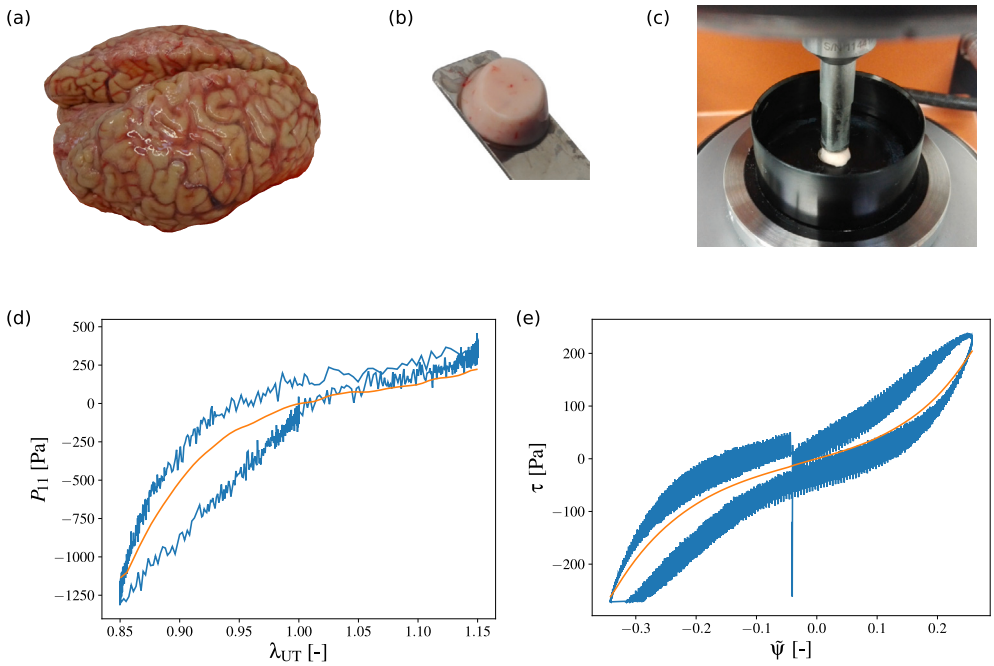

Fig. 6. Experimental setup and data preprocessing. Cylindrical samples (b) are extracted from multiple locations within the human brains (a) and then mounted to the rheometer (c). The raw data from the rheometer (blue) is preprocessed to obtain the hyperelastic response (orange) (see (d) and (e)). This is exemplarily shown for a specimen from the motor cortex (HBE_1_8). First, the noise is reduced using a moving average as well as a lowpass filter. Subsequently, the hyperelastic response is obtained by averaging the loading and unloading curve.

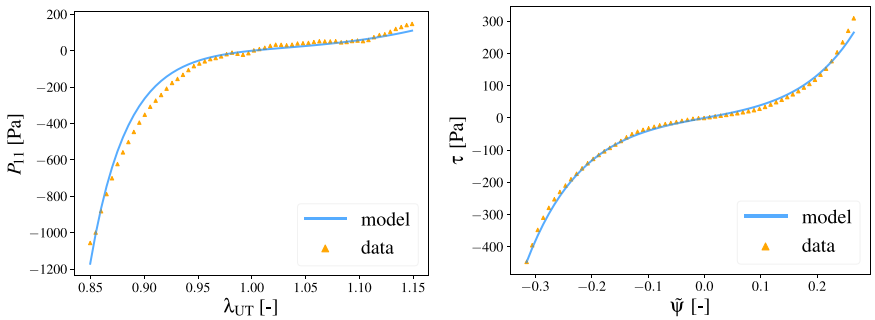

(a) HBE_01_26 under UT (b) HBE_01_26 under ST

Fig. 7. Stress versus stretch response under uniaxial compression/tension and torque versus (normalized) twist response under simple torsion of a discovered material model in comparison with the experimental data. The mean squared error $\overline{\text{MSE}} = 0.0091$ is the smallest in the data set.

true during the mechanical experiments. For example, the geometries of some of the specimens were not ideally cylindrical, because the softer specimens deformed under their own weight. Further, it was assumed throughout the derivations in this paper that the strain state in the specimens is homogeneous under uniaxial compression/tension, and it was assumed that the specimens are fixed in longitudinal direction at the boundaries, but free to move in the transversal directions. During the experiments, however, both ends of the specimens were glued, meaning that the cross-sectional area of the specimens remained unchanged at the glued boundaries. Therefore, the sides of the cylindrical specimens bulged into a barrel shape, resulting in non-homogeneous strain states in the specimens. The constraint that the specimens are fixed in both longitudinal and transversal directions may add additional stiffness to the experimentally measured stress versus stretch response, which could explain the underestimated stress by the discovered material models during uniaxial compression/tension in Fig. 8. Another source for the disagreement between the discovered models and the data could be that only isotropic material behavior has been included in the material model library. Thus, possible effects from material anisotropy in the experimental data cannot be predicted by the discovered models.

Finally, Fig. 9 shows the stretch versus stress and normalized twist versus torque plots of discovered material models for which the value of $\overline{\text{MSE}}$ is large in comparison to the other experiments. As the large mean squared error indicates, the mismatch between the discovered model and the data is significant. Such large discrepancies are exceptional for the considered experimental data

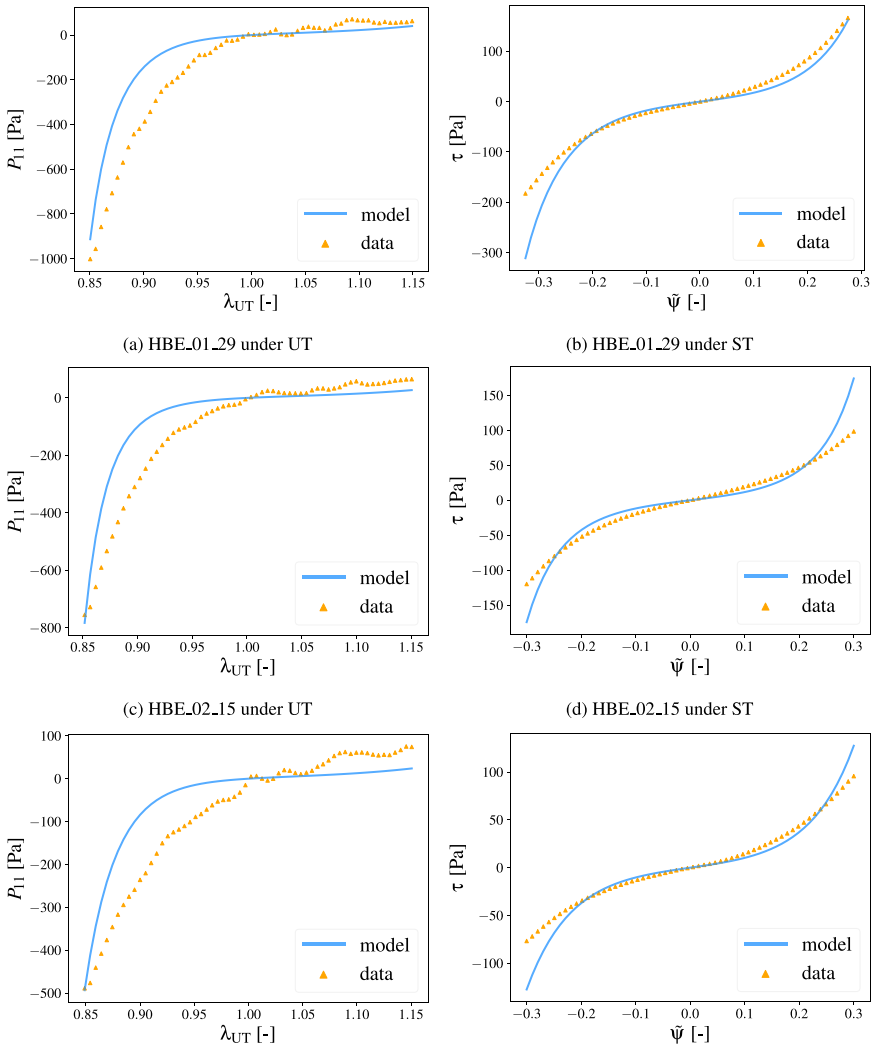

(a) HBE_01_29 under UT (b) HBE_01_29 under ST

(c) HBE_02_15 under UT (d) HBE_02_15 under ST

(e) HBE_03_15 under UT (f) HBE_03_15 under ST

Fig. 8. Stress versus stretch response under uniaxial compression/tension and torque versus (normalized) twist response under simple torsion of a discovered material model in comparison with the experimental data. The mean squared errors ($\overline{\text{MSE}} = 0.1657$, $\overline{\text{MSE}} = 0.1671$, $\overline{\text{MSE}} = 0.1664$ for HBE_01_29, HBE_02_15, HBE_03_15, respectively) are close to the average $\overline{\text{MSE}}$ in the data set.

sets (see Tables E.5 and E.6). For cyclic shear tests, the reason for the large deviation between the model and the data could be erroneous experimental measurements: the two shown samples were not loaded symmetrically during cyclic shear tests but were already twisted before the shear test started. This can happen when a torque is induced during axial loading (for example due to inhomogeneous microstructure of the sample). In this case, the rheometer applies a deformation until the torque goes back to zero. The non-monotonic stress versus stretch response under uniaxial compression/tension in Fig. 9(a) could be a consequence of a low signal-to-noise ratio since this sample is very soft. The non-increasing constant stress plateau under uniaxial compression/tension in Fig. 9(c) could indicate a failure of the glue that connects the specimen with the testing machine.

6. Conclusion

EUCLID, a recently proposed computational framework for automatically discovering constitutive models as interpretable symbolic mathematical expressions, was formulated in this work in a supervised setting and validated on the mechanical testing data of human brain specimens. It was shown that the proposed model selection strategy, which comprises sparse regression and feature clustering, is able to automatically discover interpretable constitutive models with satisfactory fitting accuracy to the given uniaxial compression/tension and simple torsion data. In contrast to previous works on discovering hyperelastic material models through sparse regression, the proposed method is able to discover models that depend nonlinearly on the material parameters like

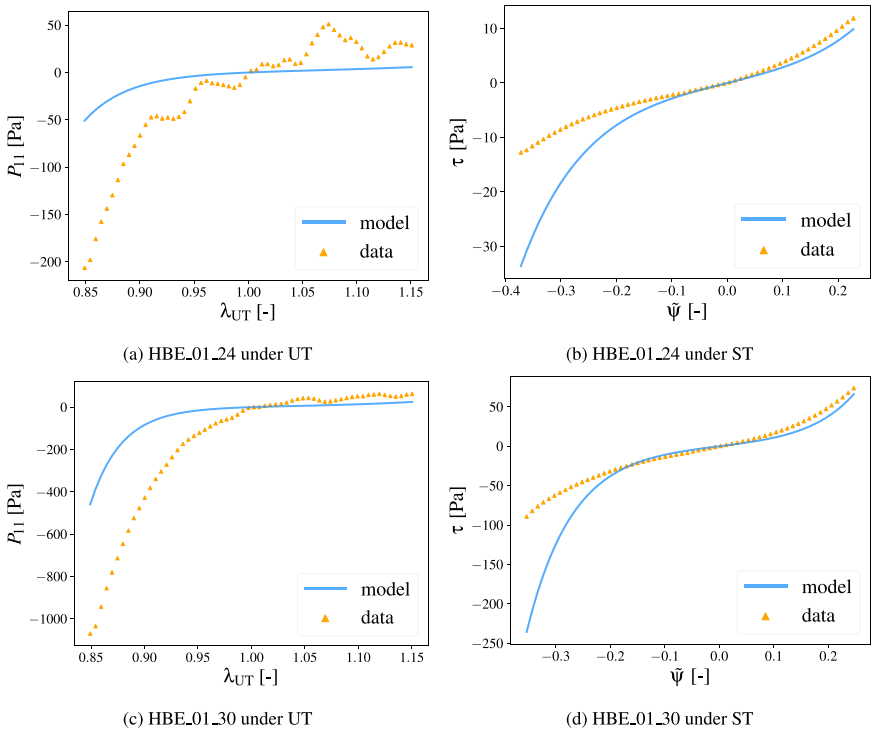

(a) HBE_01_24 under UT

(b) HBE_01_24 under ST

(c) HBE_01_30 under UT

(d) HBE_01_30 under ST

Fig. 9. Stress versus stretch response under uniaxial compression/tension and torque versus (normalized) twist response under simple torsion of discovered material models in comparison with the experimental data. The mean squared errors ($\overline{\text{MSE}} = 0.7064$, $\overline{\text{MSE}} = 0.6107$ for HBE_01_24, HBE_01_30, respectively) are the largest in the data set.

the Ogden model. This increases the expressiveness of the model library and thus the generalizability of the method to different materials. In fact, the most commonly discovered model in this work was the one-term Ogden model, which has also previously been widely used to fit human brain tissue data. The presented results constitute the first experimental validation of EUCLID. However, several aspects of the proposed method may be improved or extended in future studies. For example, the method proposed in this work is informed by labeled data pairs due to the limited access to full-field displacement data for human brain tissues. The experimental validation of EUCLID driven by unlabeled data, i.e., full-field displacement and net reaction force data (see Flaschel (2023)), is the subject of ongoing research. Moreover, we restricted the model library in which EUCLID searches for a model to the class of isotropic hyperelastic models. As the tissue response is in fact not just hyperelastic but affected by dissipative effects as well as possibly not perfectly isotropic, an important future study could be to further generalize the model library, such that EUCLID can not only select a constitutive model for the human brain tissue within a predefined class of models, but further distinguish between different modeling classes (such as hyperelasticity, viscoelasticity, elastoplasticity), as shown by Flaschel et al. (2023) for synthetical data, as well as automatically detect possible anisotropies and identify the corresponding parameters.

CRediT authorship contribution statement

Moritz Flaschel: Conceptualization, Methodology, Software, Investigation, Writing — original draft, Supervision. **Huitian Yu:** Methodology, Software, Formal analysis, Investigation, Writing – original draft. **Nina Reiter:** Resources, Data curation, Investigation, Writing – original draft. **Jan Hinrichsen:** Resources, Data curation, Investigation, Writing – original draft. **Silvia Budday:** Conceptualization, Resources, Writing – review & editing, Funding acquisition. **Paul Steinmann:** Conceptualization, Resources, Writing – review & editing, Funding acquisition. **Siddhant Kumar:** Conceptualization, Methodology, Writing – review & editing. **Laura De Lorenzis:** Conceptualization, Methodology, Writing – review & editing, Supervision, Funding acquisition.

Declaration of competing interest

The authors declare that they have no known competing financial interests or personal relationships that could have appeared to influence the work reported in this paper.

Code and data availability

Codes and data related to the EUCLID project are available at https://euclid-code.github.io/. The codes corresponding to this work are publically available in the ETH library (Yu et al., 2023) and the mechanical testing data of the human brain tissue are available upon request.

Acknowledgments

MF and LDL acknowledge funding by the Swiss National Science Foundation (SNF) through grant N. 200021_204316 "Unsupervised data-driven discovery of material laws". SB and PS acknowledge funding by the German Research Foundation (DFG) through grants N. 460333672/CRC1540/1 – 2023 "Exploring Brain Mechanics (EBM)" and BU 3728/1-1. PS acknowledges support from the European Research Council (ERC) through grant N. 101052785, "Configurational Mechanics of Soft Materials (SoftFrac)".

Code and data availability

Codes and data related to the EUCLID project are available at https://euclid-code.github.io/. The codes corresponding to this work are publically available in the ETH library (Yu et al., 2023) and the mechanical testing data of the human brain tissue are available upon request.

Appendix A. Derivatives

A.1. Derivatives of the strain invariants

The derivatives of the strain invariants with respect to the deformation gradient are

$$\frac{\partial I_1}{\partial \mathbf{F}} = 2\mathbf{F}, \quad \frac{\partial I_2}{\partial \mathbf{F}} = 2I_1\mathbf{F} - 2\mathbf{F}\mathbf{C}. \tag{A.1}$$

A.2. Derivatives of the principal stretches

The derivatives of the principal directions depend on the eigenvectors of $\mathbf{C} = \mathbf{F}^T\mathbf{F}$, denoted by $\boldsymbol{N}_i$, and the eigenvectors of $\boldsymbol{b} = \mathbf{F}\mathbf{F}^T$, denoted by $\boldsymbol{n}_i$. Under the assumption $\lambda_1 \neq \lambda_2 \neq \lambda_3 \neq \lambda_1$, it is (see Holzapfel (2000))

$$\frac{\partial \lambda_1}{\partial \mathbf{F}} = \boldsymbol{n}_1 \otimes \boldsymbol{N}_1, \quad \frac{\partial \lambda_2}{\partial \mathbf{F}} = \boldsymbol{n}_2 \otimes \boldsymbol{N}_2, \quad \frac{\partial \lambda_3}{\partial \mathbf{F}} = \boldsymbol{n}_3 \otimes \boldsymbol{N}_3. \tag{A.2}$$

A.3. Derivatives of the feature vectors

The derivatives of the feature vector $\boldsymbol{Q}_I$ with respect to the strain invariants are

$$\begin{aligned} \frac{\partial \boldsymbol{Q}_I}{\partial I_1} &= \left[m(I_1-3)^{m-1}(I_2-3)^{n-m} : n \in \{1,\dots,N_{\text{Mooney}}\}, m \in \{0,\dots,n\}\right]^T \oplus [\ 0\ ], \\ \frac{\partial \boldsymbol{Q}_I}{\partial I_2} &= \left[(n-m)(I_1-3)^{m}(I_2-3)^{n-m-1} : n \in \{1,\dots,N_{\text{Mooney}}\}, m \in \{0,\dots,n\}\right]^T \oplus \left[\ 1/I_2\ \right], \end{aligned} \tag{A.3}$$

which can be used to calculate the derivatives of the strain energy density contribution $\tilde{W}_I$ with respect to the strain invariants, i.e.,

$$\frac{\partial \tilde{W}_I}{\partial I_a} = \boldsymbol{\theta}_I \cdot \frac{\partial \boldsymbol{Q}_I}{\partial I_a}. \tag{A.4}$$

The components of the feature vector $\boldsymbol{Q}_\lambda$ are defined as

$$\left\{Q_\lambda(\lambda_1,\lambda_2,\lambda_3)\right\}_i = \lambda_1^{\alpha_i} + \lambda_2^{\alpha_i} + \lambda_3^{\alpha_i} - 3. \tag{A.5}$$

Assuming incompressibility $\lambda_1\lambda_2\lambda_3 \overset{!}{=} 1$, the components of the feature vector $\boldsymbol{Q}_\lambda$ can be written as

$$\left\{Q_\lambda(\lambda_1,\lambda_2)\right\}_i = \lambda_1^{\alpha_i} + \lambda_2^{\alpha_i} + \lambda_1^{-\alpha_i}\lambda_2^{-\alpha_i} - 3. \tag{A.6}$$

Thus, the derivatives of the components of the feature vector $\boldsymbol{Q}_\lambda$ with respect to the principal stretches are

$$\begin{aligned} \frac{\partial \left\{Q_\lambda(\lambda_1,\lambda_2)\right\}_i}{\partial \lambda_1} &= \alpha_i\left(\lambda_1^{\alpha_i-1} - \lambda_1^{-\alpha_i-1}\lambda_2^{-\alpha_i}\right), \\ \frac{\partial \left\{Q_\lambda(\lambda_1,\lambda_2)\right\}_i}{\partial \lambda_2} &= \alpha_i\left(\lambda_2^{\alpha_i-1} - \lambda_1^{-\alpha_i}\lambda_2^{-\alpha_i-1}\right), \end{aligned} \tag{A.7}$$

which can be used to calculate the derivatives of the strain energy density contribution $\tilde{W}_\lambda$ with respect to the principal stretches, i.e.,

$$\frac{\partial \tilde{W}_\lambda}{\partial \lambda_i} = \boldsymbol{\theta}_\lambda \cdot \frac{\partial \boldsymbol{Q}_\lambda}{\partial \lambda_i}. \tag{A.8}$$

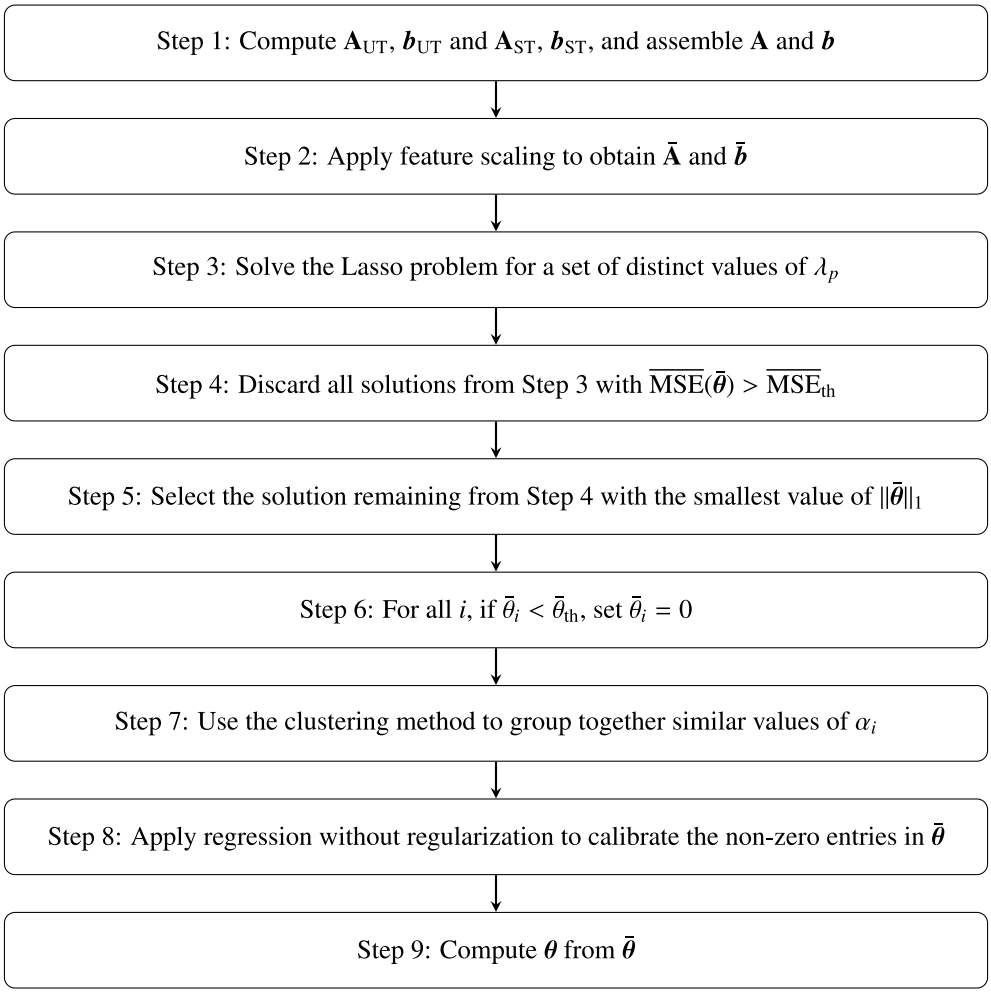

Fig. B.10. Step-by-step description of the sparsity promoting algorithm for material model discovery.

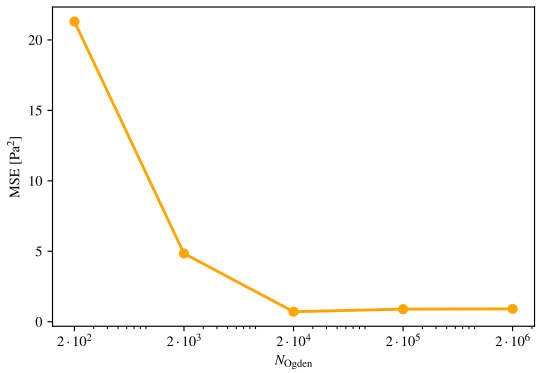

Fig. C.11. Relation between the choice of N_{Ogden} and the MSE.

A.4. Derivatives for uniaxial compression and tension

In the following, we seek to simplify the expression for $P_{11}(\lambda_{\mathrm{UT}};\boldsymbol{\theta})$ (see Eq. (16)) by leveraging the characteristics of the kinematic state under uniaxial compression and tension. Considering such kinematic state, the deformation gradient and the resulting right

Table C.2
Effect of the choice of N_{Ogden} on the solution of the inverse problem.

N_{Ogden}	MSE [Pa^2]	Time [s]	α	μ
Truth	–	–	−12.1351	147.2617
$2 \cdot 10^2$	21.30679	120.6681	−12	153.411
$2 \cdot 10^3$	4.844132	171.5938	−12.2	144.3845
$2 \cdot 10^4$	0.713393	708.2161	−12.16	146.1534
$2 \cdot 10^5$	0.89581	6107.209	−12.163	146.0201
$2 \cdot 10^6$	0.91519	60 267.82	−12.1633	146.0068

Table D.3
Heights and regions of the brain tissue specimens.

HBE	Region	h [mm]	HBE	Region	h [mm]	HBE	Region	h [mm]	HBE	Region	h [mm]
01_03	C	4.89159	02_01	CR	2.9083	03_01	BS	6.1803	03_21	CC	4.32991
01_04	BG	4.44005	02_02	C	4.36397	03_02	BS	5.17463	03_22	CC	3.91166
01_05	CR	4.64004	02_03	C	3.56882	03_03	BS	6.52776	03_23	CR	5.91647
01_06	CR	4.19198	02_04	CR	3.70545	03_04	Am	4.04604	03_25	C	4.7642
01_07	BG	3.86355	02_05	CC	3.71248	03_05	M	5.39193	03_26	Am	4.79861
01_08	C	5.1278	02_06	CC	4.27716	03_06	M	5.20739	03_27	BG	5.46595
01_09	BG	3.6299	02_07	CC	3.8597	03_07	CC	3.7975	03_28	BG	5.80823
01_10	CR	3.79468	02_08	CC	4.0629	03_08	CC	4.29526	03_29	CR	5.61761
01_12	CC	4.29779	02_09	M	5.16654	03_09	BG	5.64718	03_30	CR	4.97806
01_13	CR	3.89796	02_10	BG	4.00143	03_10	BG	4.96097	03_31	C	4.68306
01_14	C	4.59097	02_13	M	5.28094	03_11	CC	5.15737	03_32	CR	4.01945
01_21	C	4.42721	02_14	BG	4.84645	03_12	BG	5.96805	03_33	CR	6.07937
01_22	CR	3.7167	02_15	BG	4.69894	03_13	CC	3.27287	03_34	CR	4.66727
01_23	C	3.78048	02_16	CR	4.96181	03_14	CB	6.77129	03_35	CR	5.81572
01_24	CR	2.79804	02_17	C	4.63	03_15	CB	6.74769	03_36	C	3.8775
01_25	BS	3.61422	02_18	BG	3.91647	03_16	CB	6.40546	03_37	M	5.80837
01_26	BS	4.11383	02_19	C	4.79345	03_17	CB	5.18112	03_38	M	6.11145
01_27	CB	4.9045	02_20	BS	5.41687	03_18	CR	6.19653	03_39	C	4.75102
01_28	CB	4.6799	02_21	BS	4.36067	03_19	C	4.86192	03_40	CR	5.26147
01_29	M	3.121	02_22	CB	5.37975	03_20	BG	6.97399	03_41	C	4.96854
01_30	M	4.74689									

Table D.4
Abbreviations and full names of the brain regions.

Am	Amygdala	BG	Basal ganglia	BS	Brain stem	C	Cortex
CB	Cerebellum	CC	Corpus callosum	CR	Corona radiata	M	Midbrain

Cauchy–Green strain tensor read

$$\mathbf{F} = \begin{bmatrix} \lambda_{\text{UT}} & 0 & 0 \\ 0 & \frac{1}{\sqrt{\lambda_{\text{UT}}}} & 0 \\ 0 & 0 & \frac{1}{\sqrt{\lambda_{\text{UT}}}} \end{bmatrix}, \qquad \mathbf{C} = \begin{bmatrix} \lambda_{\text{UT}}^2 & 0 & 0 \\ 0 & \frac{1}{\lambda_{\text{UT}}} & 0 \\ 0 & 0 & \frac{1}{\lambda_{\text{UT}}} \end{bmatrix}. \tag{A.9}$$

Thus, the strain invariants simplify to

$$I_1 = \lambda_{\text{UT}}^2 + \frac{2}{\lambda_{\text{UT}}}, \quad I_2 = 2\lambda_{\text{UT}} + \frac{1}{\lambda_{\text{UT}}^2}, \tag{A.10}$$

and the principal stretches simplify to

$$\lambda_1 = \lambda_{\text{UT}}, \quad \lambda_2 = \lambda_3 = \frac{1}{\sqrt{\lambda_{\text{UT}}}}. \tag{A.11}$$

The simple structure of the kinematic state is used to simplify the feature vector $\boldsymbol{Q}$. The feature vectors $\boldsymbol{Q}_I$ and $\boldsymbol{Q}_\lambda$ are

$$\boldsymbol{Q}_I(\lambda_{\text{UT}}) = \left[\left(\lambda_{\text{UT}} - 3\right)^m \left(2\lambda_{\text{UT}} + \frac{1}{\lambda_{\text{UT}}^2} - 3\right)^{n-m} : n \in \{1, \dots, N_{\text{Mooney}}\}, m \in \{0, \dots, n\} \right]^T \oplus \left[\log\left(\frac{2}{3}\lambda_{\text{UT}} + \frac{1}{3\lambda_{\text{UT}}^2}\right) \right], \tag{A.12}$$

and

$$\left\{Q_\lambda(\lambda_{\text{UT}})\right\}_i = \lambda_{\text{UT}}^{\alpha_i} + 2\left(\frac{1}{\sqrt{\lambda_{\text{UT}}}}\right)^{\alpha_i} - 3, \tag{A.13}$$

Table E.5
Material parameters, mean squared errors and time to solution for the material model discovery from experimental data — brain no. 01 and 02. Note that model parameters that are zero throughout all experiments are not shown in the table. All material parameters are in Pa, except for the dimensionless parameters α_i.

HBE	Material parameters								MSE	$\overline{\text{MSE}}$	Time
	μ_1	α_1	μ_2	α_2	I_2-3	$(I_2-3)^2$	$(I_2-3)(I_1-3)$	$(I_1-3)^2$	[Pa^2]	[−]	[s]
01_03	29.85	−38.84	–	–	–	–	–	–	1364.68	0.26	688
01_04	125.13	−21.14	–	–	–	–	–	–	260.16	0.08	713
01_05	0.13	−68.28	6.64	−33.86	–	–	–	–	373.01	0.51	718
01_06	–	–	–	–	33.50	–	–	–	189.60	0.50	638
01_07	7.38	−49.08	69.29	−25.57	–	–	–	–	2861.05	0.27	719
01_08	350.45	−18.80	–	–	–	–	–	–	1327.16	0.07	741
01_09	122.55	−25.75	–	–	–	–	–	–	878.70	0.14	715
01_10	1.80	−57.89	–	–	–	–	–	–	1027.67	0.43	666
01_12	33.75	−20.06	–	–	–	–	–	–	16.97	0.09	680
01_13	0.85	−54.19	49.02	−23.15	–	–	–	–	251.27	0.18	670
01_14	274.80	−21.10	–	–	–	–	–	–	606.65	0.04	680
01_21	2.09	−54.38	10.20	−24.62	–	–	–	–	872.84	0.49	675
01_22	2.46	−45.70	45.62	−25.99	–	–	–	–	291.84	0.16	674
01_23	35.76	−36.88	–	–	–	–	–	–	983.44	0.23	790
01_24	16.35	−20.05	–	–	–	–	–	–	140.42	0.71	684
01_25	0.10	−70.62	62.52	−25.82	–	–	–	–	540.38	0.18	717
01_26	207.64	−24.58	–	–	–	392.93	–	–	136.29	0.01	758
01_27	2.37	−52.66	64.85	−24.86	–	–	–	–	970.58	0.23	708
01_28	119.72	−18.48	–	–	–	160.40	–	–	46.12	0.02	727
01_29	0.01	−78.58	90.36	−28.71	–	–	–	–	1138.84	0.17	781
01_30	55.97	−28.04	–	–	–	–	–	–	3227.89	0.61	743
02_01	6.03	−51.39	–	–	–	–	–	–	1499.17	0.35	816
02_02	1.37	−51.25	76.88	−22.85	–	–	–	–	275.26	0.11	816
02_03	56.66	−34.54	–	–	–	–	–	–	1369.33	0.20	750
02_04	9.11	−46.83	–	–	–	–	–	–	1014.31	0.32	767
02_05	1.06	−51.48	16.30	−21.06	–	–	–	–	64.85	0.20	700
02_06	0.37	−46.55	16.32	−24.76	–	–	–	–	26.25	0.18	686
02_07	53.93	−18.72	–	–	–	–	–	–	20.69	0.05	710
02_08	0.49	−50.67	42.52	−10.72	–	–	–	–	42.58	0.18	730
02_09	134.96	−25.83	–	–	–	280.13	–	–	211.21	0.03	763
02_10	7.25	−47.26	–	–	–	–	–	–	808.74	0.34	692
02_13	0.94	−51.11	72.32	−25.43	–	–	–	–	272.57	0.10	746
02_14	92.21	−24.97	–	–	–	–	–	–	166.90	0.06	766
02_15	2.21	−52.14	58.47	−26.20	–	–	–	–	591.73	0.17	837
02_16	3.88	−46.16	19.90	−28.55	–	–	–	–	334.23	0.24	723
02_17	7.69	−44.42	19.19	−29.34	–	–	–	–	1013.33	0.34	692
02_18	88.59	−22.14	–	–	–	–	–	–	92.16	0.06	732
02_19	28.46	−37.27	–	–	–	–	–	–	746.94	0.23	754
02_20	4.99	−46.94	18.22	−25.82	–	–	–	–	363.63	0.22	784
02_21	73.98	−24.99	–	–	–	–	–	–	117.98	0.07	751
02_22	2.96	−48.92	25.56	−24.22	–	–	–	–	298.52	0.24	731

whose derivatives with respect to λ_{UT} are trivial. We finally obtain the following expression for the feature vector derivative in Eq. (16)

$$\boldsymbol{Q}'_{\text{UT}}(\lambda_{\text{UT}}) = \frac{\partial \boldsymbol{Q}(\lambda_{\text{UT}})}{\partial \lambda_{\text{UT}}}, \tag{A.14}$$

which after substitution in Eq. (16) results in a simplified expression for $P_{11}(\lambda_{\text{UT}};\boldsymbol{\theta})$.

A.5. Derivatives for simple torsion

In the following, we seek to simplify the expression for $\tau(\tilde{\psi};\boldsymbol{\theta})$ (see Eq. (21)) by leveraging the characteristics of the kinematic state under simple torsion. Considering simple torsion, the deformation gradient and the resulting right Cauchy–Green strain tensor read

$$\mathbf{F} = \begin{bmatrix} 1 & 0 & 0 \\ 0 & 1 & F_{\vartheta z} \\ 0 & 0 & 1 \end{bmatrix}, \qquad \mathbf{C} = \begin{bmatrix} 1 & 0 & 0 \\ 0 & 1 & F_{\vartheta z} \\ 0 & F_{\vartheta z} & 1+F_{\vartheta z}^2 \end{bmatrix}, \tag{A.15}$$

where $F_{\vartheta z} = \rho\tilde{\psi}$. Thus, the strain invariants simplify to

$$I_1 = I_2 = F_{\vartheta z}^2 + 3. \tag{A.16}$$

Table E.6
Material parameters, mean squared errors and time to solution for the material model discovery from experimental data — brain no. 03. Note that model parameters that are zero throughout all experiments are not shown in the table. All material parameters are in Pa, except for the dimensionless parameters α_i.

HBE	Material parameters								MSE	$\overline{\text{MSE}}$	Time
	μ_1	α_1	μ_2	α_2	I_2-3	$(I_2-3)^2$	$(I_2-3)(I_1-3)$	$(I_1-3)^2$	[Pa^2]	[−]	[s]
03_01	4.13	−46.12	43.08	−26.43	–	–	–	–	548.09	0.20	703
03_02	38.05	−19.71	–	–	–	–	–	–	9.05	0.04	694
03_03	33.32	−30.51	–	–	–	–	–	–	105.64	0.11	793
03_04	4.24	−43.24	63.20	−23.46	–	–	–	–	241.05	0.10	753
03_05	85.82	−22.43	–	–	–	–	–	–	77.84	0.05	710
03_06	71.81	−28.86	–	–	–	–	–	–	123.95	0.04	717
03_07	0.53	−50.57	12.87	−22.03	–	–	–	–	19.29	0.16	709
03_08	0.97	−48.88	12.33	−17.28	–	–	–	–	30.73	0.22	711
03_09	95.08	−20.61	–	–	–	–	–	–	33.18	0.02	726
03_10	22.46	−30.21	–	–	–	–	–	–	58.02	0.13	776
03_11	52.98	−16.10	–	–	–	–	–	–	4.30	0.02	708
03_12	55.48	−29.03	–	–	–	–	–	–	183.62	0.09	744
03_13	8.98	−11.23	–	–	–	–	41.30	–	3.30	0.04	685
03_14	5.19	−41.87	–	–	–	–	–	–	86.43	0.30	767
03_15	52.15	−29.04	–	–	–	–	–	–	344.86	0.17	702
03_16	4.14	−42.41	–	–	–	–	–	–	77.03	0.33	697
03_17	22.37	−34.83	–	–	–	–	–	–	212.28	0.18	700
03_18	52.44	−18.07	–	–	–	–	–	–	7.86	0.02	725
03_19	35.71	−27.60	–	–	–	–	–	–	76.98	0.11	708
03_20	69.96	−24.83	–	–	–	–	–	–	181.74	0.11	719
03_21	6.67	−33.26	–	–	–	–	–	–	8.02	0.12	748
03_22	23.35	−19.87	–	–	–	–	–	102.69	7.63	0.05	781
03_23	4.50	−46.22	11.66	−26.94	–	–	–	–	295.75	0.26	737
03_25	63.51	−29.29	–	–	–	–	–	–	366.86	0.13	795
03_26	62.21	−20.92	–	–	–	–	–	–	45.17	0.06	770
03_27	68.54	−23.96	–	–	–	–	–	–	70.19	0.05	764
03_28	191.05	−18.54	–	–	–	–	–	–	50.77	0.01	740
03_29	1.84	−51.56	28.07	−19.34	–	–	–	–	388.02	0.35	693
03_30	58.05	−21.27	–	–	–	–	–	–	28.16	0.04	688
03_31	15.53	−40.39	–	–	–	–	–	–	478.73	0.25	728
03_32	32.07	−25.14	–	–	–	–	–	–	23.06	0.06	730
03_33	54.99	−23.71	–	–	–	–	–	–	45.31	0.05	745
03_34	1.21	−48.04	42.59	−24.79	–	–	–	–	115.99	0.12	742
03_35	29.28	−25.46	–	–	–	–	–	–	28.11	0.09	775
03_36	34.02	−32.20	–	–	–	–	–	–	345.65	0.21	760
03_37	105.48	−23.43	–	–	–	–	–	–	131.43	0.05	766
03_38	81.85	−22.01	–	–	–	–	–	–	49.05	0.03	725
03_39	83.47	−26.77	–	–	–	–	–	–	237.35	0.08	693
03_40	42.47	−23.87	–	–	–	–	–	–	22.89	0.05	692
03_41	2.90	−41.58	46.88	−29.99	–	–	–	–	365.95	0.13	677
								Average	**399.57**	**0.17**	**729**

Defining the auxiliary variable $\bar{C} = 1 + \frac{1}{2}F_{\vartheta z}^2$, the eigenvalues of $\mathbf{C}$ (which are the squares of the principal stretches) read

$$\lambda_1^2 = \bar{C} - \sqrt{\bar{C}^2 - 1}, \quad \lambda_2^2 = 1, \quad \lambda_3^2 = \bar{C} + \sqrt{\bar{C}^2 - 1}, \tag{A.17}$$

which results in the principal stretches

$$\lambda_1 = \sqrt{\bar{C} - \sqrt{\bar{C}^2 - 1}}, \quad \lambda_2 = 1, \quad \lambda_3 = \sqrt{\bar{C} + \sqrt{\bar{C}^2 - 1}}. \tag{A.18}$$

The simple structure of the kinematic state is used to simplify the feature vector $\boldsymbol{Q}$. The feature vector $\boldsymbol{Q}_I$ is

$$\boldsymbol{Q}_I(F_{\vartheta z}) = \left[F_{\vartheta z}^{2n} : n \in \{1, \dots, N_{\text{Mooney}}\}, m \in \{0, \dots, n\}\right]^T \oplus \left[\log\left(F_{\vartheta z}^2/3 + 1\right)\right], \tag{A.19}$$

whose derivative with respect to $F_{\vartheta z}$ is trivial, and the feature vector $\boldsymbol{Q}_\lambda$ is

$$\left\{Q_\lambda(\bar{C})\right\}_i = \left(\sqrt{\bar{C} - \sqrt{\bar{C}^2 - 1}}\right)^{\alpha_i} + \left(\sqrt{\bar{C} + \sqrt{\bar{C}^2 - 1}}\right)^{\alpha_i} - 2, \tag{A.20}$$

whose derivative with respect to $F_{\vartheta z}$ can be computed using the chain rule

$$\frac{\partial \boldsymbol{Q}_\lambda}{\partial F_{\vartheta z}} = \frac{\partial \boldsymbol{Q}_\lambda}{\partial \bar{C}} \frac{\partial \bar{C}}{\partial F_{\vartheta z}} = \frac{\partial \boldsymbol{Q}_\lambda}{\partial \bar{C}} F_{\vartheta z}. \tag{A.21}$$

Thus, the derivative $\frac{\partial \boldsymbol{Q}}{\partial F_{\vartheta z}}$ is known and it depends on ρ and $\tilde{\psi}$ through $\bar{C} = 1 + \frac{1}{2}F_{\vartheta z}^2$ and $F_{\vartheta z} = \rho\tilde{\psi}$. With reference to Eq. (21), it is

$$\boldsymbol{Q}'_{\mathrm{ST}}(\tilde{\psi}) = \int_0^1 2\pi\rho^2 \frac{\partial \boldsymbol{Q}}{\partial F_{\vartheta z}} \, \mathrm{d}\rho, \tag{A.22}$$

where the integral over ρ can be computed through numerical quadrature.

Appendix B. Algorithm

Fig. B.10 provides a step-by-step description of the proposed algorithm for material model discovery.

Appendix C. Effect of the choice of candidate values of α_i on the expressiveness of the model library

In the following, we numerically investigate the effect of the choice of candidate values of α_i on the expressiveness of the model library. To this end, we generate synthetical data for the one-term Ogden model, $W = \frac{2\mu}{\alpha^2}\left(\lambda_1^\alpha + \lambda_2^\alpha + \lambda_3^\alpha - 3\right)$, as described Section 4. Note that in contrast to Section 4, we purposefully choose non-integer numbers for the ground truth parameters, i.e., $\mu = 147.2617\mathrm{Pa}$ and $\alpha = -12.1351$. Afterwards, the effect of the choice of candidate values of α_i on the inverse problem is studied by solving the inverse problem (see Section 3) for different choices of candidate values of α_i. As in Section 2, we choose N_{Ogden} values of α_i evenly distributed between -100 and 100 excluding zero and solve the problem for different choices of N_{Ogden}, i.e., $N_{\mathrm{Ogden}} \in \{2 \cdot 10^2, 2 \cdot 10^3, 2 \cdot 10^4, 2 \cdot 10^5, 2 \cdot 10^6\}$. After solving each inverse problem, the corresponding MSE (see Section 3) is computed.

Fig. C.11 shows the relation between the choice of N_{Ogden} and the MSE. As we have chosen non-integer numbers for the ground truth parameters, the ground truth value of α is not contained in the constructed sets of candidate values of α_i if N_{Ogden} is small. Thus, the MSE is large if N_{Ogden} is small. As expected, the MSE decreases upon increasing N_{Ogden}. The MSE reaches a plateau at $N_{\mathrm{Ogden}} = 2 \cdot 10^4$, which indicates that adding more than $N_{\mathrm{Ogden}} = 2 \cdot 10^4$ candidate values of α_i to the model library does not noticeably increase the expressiveness of the model library. Table C.2 shows the MSE and the computing times of the inverse problem for the different choices of the model library. Considering that the computing time increases upon increasing N_{Ogden}, we observe that choosing $N_{\mathrm{Ogden}} = 2 \cdot 10^4$ provides a good compromise between the expressiveness of the model library and the computational cost.

Appendix D. Specimen information

The corresponding heights and regions of the different specimens are recorded in Table D.3, while the radius of each specimen is $r_{\mathrm{out}} \approx 4$ mm. Table D.4 lists the abbreviations of the brain regions and their meaning (see Hinrichsen et al. (2022)).

Appendix E. Material parameters

The discovered material models and the corresponding parameters are reported in Tables E.5 and E.6. The tables further record different measures for the fitting accuracy of the discovered models as well as the computational time needed for the discovery process.

References

Abdusalamov, R., Hillgärtner, M., Itskov, M., 2023. Automatic generation of interpretable hyperelastic material models by symbolic regression. Internat. J. Numer. Methods Engrg. nme.7203. http://dx.doi.org/10.1002/nme.7203, URL: https://onlinelibrary.wiley.com/doi/10.1002/nme.7203.

As'ad, F., Avery, P., Farhat, C., 2022. A mechanics-informed artificial neural network approach in data-driven constitutive modeling. In: AIAA SCITECH 2022 Forum. American Institute of Aeronautics and Astronautics, San Diego, CA & Virtual, http://dx.doi.org/10.2514/6.2022-0100, URL: https://arc.aiaa.org/doi/10.2514/6.2022-0100.

As'ad, F., Farhat, C., 2022. A mechanics-informed neural network framework for data-driven nonlinear viscoelasticity. http://dx.doi.org/10.13140/RG.2.2.21694.36168, URL: https://rgdoi.net/10.13140/RG.2.2.21694.36168. Publisher: Unpublished.

Bomarito, G., Townsend, T., Stewart, K., Esham, K., Emery, J., Hochhalter, J., 2021. Development of interpretable, data-driven plasticity models with symbolic regression. Comput. Struct. 252, 106557. http://dx.doi.org/10.1016/j.compstruc.2021.106557, URL: https://linkinghub.elsevier.com/retrieve/pii/S0045794921000791.

Boyce, M.C., Arruda, E.M., 2000. Constitutive models of rubber elasticity: A review. Rubber Chem. Technol. 73 (3), 504–523. http://dx.doi.org/10.5254/1.3547602, URL: https://meridian.allenpress.com/rct/article/73/3/504/92749/Constitutive-Models-of-Rubber-Elasticity-A-Review.

Brunton, S.L., Proctor, J.L., Kutz, J.N., 2016. Discovering governing equations from data by sparse identification of nonlinear dynamical systems. Proc. Natl. Acad. Sci. 113 (15), 3932–3937. http://dx.doi.org/10.1073/pnas.1517384113, URL: http://www.pnas.org/lookup/doi/10.1073/pnas.1517384113.

Budday, S., Ovaert, T.C., Holzapfel, G.A., Steinmann, P., Kuhl, E., 2020. Fifty shades of brain: A review on the mechanical testing and modeling of brain tissue. Arch. Comput. Methods Eng. 27 (4), 1187–1230. http://dx.doi.org/10.1007/s11831-019-09352-w, URL: http://link.springer.com/10.1007/s11831-019-09352-w.

Budday, S., Sommer, G., Birkl, C., Langkammer, C., Haybaeck, J., Kohnert, J., Bauer, M., Paulsen, F., Steinmann, P., Kuhl, E., Holzapfel, G., 2017. Mechanical characterization of human brain tissue. Acta Biomater. 48, 319–340. http://dx.doi.org/10.1016/j.actbio.2016.10.036, URL: https://linkinghub.elsevier.com/retrieve/pii/S1742706116305633.

Chen, P., Guilleminot, J., 2022. Polyconvex neural networks for hyperelastic constitutive models: A rectification approach. Mech. Res. Commun. 125, 103993. http://dx.doi.org/10.1016/j.mechrescom.2022.103993, URL: https://linkinghub.elsevier.com/retrieve/pii/S0093641322001252.

Dal, H., Açıkgöz, K., Badienia, Y., 2021. On the performance of isotropic hyperelastic constitutive models for rubber-like materials: A state of the art review. Appl. Mech. Rev. 73 (2), 020802. http://dx.doi.org/10.1115/1.4050978, URL: https://asmedigitalcollection.asme.org/appliedmechanicsreviews/article/73/2/020802/1108153/On-the-Performance-of-Isotropic-Hyperelastic.

Efron, B., Hastie, T., Johnstone, I., Tibshirani, R., 2004. Least angle regression. Ann. Statist. 32 (2), 407–499.

Ester, M., Kriegel, H.-P., Xu, X., 1996. A density-based algorithm for discovering clusters in large spatial databases with noise. In: Proceedings of the 2nd International Conference on Knowledge Discovery and Data Mining, Portland. pp. 226–231.

Faber, J., Hinrichsen, J., Greiner, A., Reiter, N., Budday, S., 2022. Tissue-scale biomechanical testing of brain tissue for the calibration of nonlinear material models. Curr. Protoc. 2 (4), e381. http://dx.doi.org/10.1002/cpz1.381, Publisher: John Wiley & Sons, Ltd.

Flaschel, M., 2023. Automated Discovery of Material Models in Continuum Solid Mechanics (Ph.D. thesis). ETH Zurich, http://dx.doi.org/10.3929/ETHZ-B-000602750, URL: http://hdl.handle.net/20.500.11850/602750.

Flaschel, M., Kumar, S., De Lorenzis, L., 2021. Unsupervised discovery of interpretable hyperelastic constitutive laws. Comput. Methods Appl. Mech. Engrg. 381, 113852. http://dx.doi.org/10.1016/j.cma.2021.113852.

Flaschel, M., Kumar, S., De Lorenzis, L., 2022. Discovering plasticity models without stress data. NPJ Comput. Mater. 8 (1), 91. http://dx.doi.org/10.1038/s41524-022-00752-4, URL: https://www.nature.com/articles/s41524-022-00752-4.

Flaschel, M., Kumar, S., De Lorenzis, L., 2023. Automated discovery of generalized standard material models with EUCLID. Comput. Methods Appl. Mech. Engrg. 405, 115867. http://dx.doi.org/10.1016/j.cma.2022.115867, URL: https://linkinghub.elsevier.com/retrieve/pii/S0045782522008234.

Frank, I.E., Friedman, J.H., 1993. A statistical view of some chemometrics regression tools. Technometrics 35 (2), 109–135. http://dx.doi.org/10.1080/00401706.1993.10485033, URL: http://www.tandfonline.com/doi/abs/10.1080/00401706.1993.10485033.

Frankel, A.L., Jones, R.E., Swiler, L.P., 2020. Tensor basis gaussian process models of hyperelastic materials. J. Mach. Learn. Model. Comput. 1 (1), 1–17. http://dx.doi.org/10.1615/JMachLearnModelComput.2020033325, URL: http://www.dl.begellhouse.com/journals/558048804a15188a,583c4e56625ba94e,651a2e6b0260f708.html.

Friedman, J., Hastie, T., Tibshirani, R., 2010. Regularization paths for generalized linear models via coordinate descent. J. Stat. Softw. 33 (1), http://dx.doi.org/10.18637/jss.v033.i01, URL: http://www.jstatsoft.org/v33/i01/.

Gent, A.N., Thomas, A.G., 1958. Forms for the stored (strain) energy function for vulcanized rubber. J. Polym. Sci. 28 (118), 625–628. http://dx.doi.org/10.1002/pol.1958.1202811814, URL: http://doi.wiley.com/10.1002/pol.1958.1202811814.

Ghaboussi, J., Garrett, J.H., Wu, X., 1991. Knowledge-based modeling of material behavior with neural networks. J. Eng. Mech. 117 (1), 132–153. http://dx.doi.org/10.1061/(ASCE)0733-9399(1991)117:1(132), URL: http://ascelibrary.org/doi/10.1061/%28ASCE%290733-9399%281991%29117%3A1%28132%29.

Hartmann, S., 2001. Parameter estimation of hyperelasticity relations of generalized polynomial-type with constraint conditions. Int. J. Solids Struct. 38 (44–45), 7999–8018. http://dx.doi.org/10.1016/S0020-7683(01)00018-X, URL: https://linkinghub.elsevier.com/retrieve/pii/S002076830100018X.

He, H., Zhang, Q., Zhang, Y., Chen, J., Zhang, L., Li, F., 2021. A comparative study of 85 hyperelastic constitutive models for both unfilled rubber and highly filled rubber nanocomposite material. Nano Mater. Sci. S2589965121000490. http://dx.doi.org/10.1016/j.nanoms.2021.07.003, URL: https://linkinghub.elsevier.com/retrieve/pii/S2589965121000490.

Hinrichsen, J., Reiter, N., Bräuer, L., Paulsen, F., Kaessmair, S., Budday, S., 2022. Inverse identification of region-specific hyperelastic material parameters for human brain tissue. http://dx.doi.org/10.1101/2022.12.19.521022, URL: http://biorxiv.org/lookup/doi/10.1101/2022.12.19.521022.

Holzapfel, G.A., 2000. Nonlinear Solid Mechanics: A Continuum Approach for Engineering. Wiley, Chichester ; New York.

Ibañez, R., Abisset-Chavanne, E., Aguado, J.V., Gonzalez, D., Cueto, E., Chinesta, F., 2018. A manifold learning approach to data-driven computational elasticity and inelasticity. Arch. Comput. Methods Eng. 25 (1), 47–57. http://dx.doi.org/10.1007/s11831-016-9197-9, URL: http://link.springer.com/10.1007/s11831-016-9197-9.

Joshi, A., Thakolkaran, P., Zheng, Y., Escande, M., Flaschel, M., De Lorenzis, L., Kumar, S., 2022. Bayesian-EUCLID: Discovering hyperelastic material laws with uncertainties. Comput. Methods Appl. Mech. Engrg. 398, 115225. http://dx.doi.org/10.1016/j.cma.2022.115225, URL: https://linkinghub.elsevier.com/retrieve/pii/S0045782522003681.

Kabliman, E., Kolody, A.H., Kronsteiner, J., Kommenda, M., Kronberger, G., 2021. Application of symbolic regression for constitutive modeling of plastic deformation. Appl. Eng. Sci. 6, 100052. http://dx.doi.org/10.1016/j.apples.2021.100052, URL: https://linkinghub.elsevier.com/retrieve/pii/S2666496821000182.

Kalina, K.A., Linden, L., Brummund, J., Metsch, P., Kästner, M., 2022. Automated constitutive modeling of isotropic hyperelasticity based on artificial neural networks. Comput. Mech. 69 (1), 213–232. http://dx.doi.org/10.1007/s00466-021-02090-6, URL: https://link.springer.com/10.1007/s00466-021-02090-6.

Kirchdoerfer, T., Ortiz, M., 2016. Data-driven computational mechanics. Comput. Methods Appl. Mech. Engrg. 304, 81–101. http://dx.doi.org/10.1016/j.cma.2016.02.001, URL: https://linkinghub.elsevier.com/retrieve/pii/S0045782516300238.

Klein, D.K., Fernández, M., Martin, R.J., Neff, P., Weeger, O., 2022a. Polyconvex anisotropic hyperelasticity with neural networks. J. Mech. Phys. Solids 159, 104703. http://dx.doi.org/10.1016/j.jmps.2021.104703, URL: https://linkinghub.elsevier.com/retrieve/pii/S0022509621003215.

Klein, D.K., Ortigosa, R., Martínez-Frutos, J., Weeger, O., 2022b. Finite electro-elasticity with physics-augmented neural networks. Comput. Methods Appl. Mech. Engrg. 400, 115501. http://dx.doi.org/10.1016/j.cma.2022.115501, URL: https://linkinghub.elsevier.com/retrieve/pii/S004578252200514X.

Linka, K., Kuhl, E., 2022. A new family of constitutive artificial neural networks towards automated model discovery. URL: http://arxiv.org/abs/2210.02202. arXiv:2210.02202 [cond-mat].

Linka, K., Reiter, N., Würges, J., Schicht, M., Bräuer, L., Cyron, C.J., Paulsen, F., Budday, S., 2021. Unraveling the local relation between tissue composition and human brain mechanics through machine learning. Front. Bioeng. Biotechnol. 9, 704738. http://dx.doi.org/10.3389/fbioe.2021.704738, URL: https://www.frontiersin.org/articles/10.3389/fbioe.2021.704738/full.

Linka, K., St. Pierre, S.R., Kuhl, E., 2023. Automated model discovery for human brain using constitutive artificial neural networks. Acta Biomater. 160, 134–151. http://dx.doi.org/10.1016/j.actbio.2023.01.055, URL: https://linkinghub.elsevier.com/retrieve/pii/S1742706123000661.

Marckmann, G., Verron, E., 2006. Comparison of hyperelastic models for rubber-like materials. Rubber Chem. Technol. 79 (5), 835–858. http://dx.doi.org/10.5254/1.3547969, URL: https://meridian.allenpress.com/rct/article/79/5/835/93139/Comparison-of-Hyperelastic-Models-for-RubberLike.

Marino, E., Flaschel, M., Kumar, S., De Lorenzis, L., 2023. Automated identification of linear viscoelastic constitutive laws with EUCLID. Mech. Mater. 181, 104643. http://dx.doi.org/10.1016/j.mechmat.2023.104643, URL: https://linkinghub.elsevier.com/retrieve/pii/S0167663623000893.

Meyer, K.A., Ekre, F., 2023. Thermodynamically consistent neural network plasticity modeling and discovery of evolution laws. http://dx.doi.org/10.31224/2961, URL: https://engrxiv.org/preprint/view/2961.

Ogden, R.W., 1972. Large deformation isotropic elasticity – on the correlation of theory and experiment for incompressible rubberlike solids. Proc. R. Soc. Lond. Ser. A Math. Phys. Sci. (326), 565–584.

Park, H., Cho, M., 2021. Multiscale constitutive model using data–driven yield function. Composites B 216, 108831. http://dx.doi.org/10.1016/j.compositesb.2021.108831, URL: https://linkinghub.elsevier.com/retrieve/pii/S1359836821002225.

Rivlin, R.S., 1947. Torsion of a rubber cylinder. J. Appl. Phys. 18 (444), 7.

St. Pierre, S.R., Linka, K., Kuhl, E., 2023. Principal-stretch-based constitutive neural networks autonomously discover a subclass of ogden models for human brain tissue. Brain Multiphys. 4, 100066. http://dx.doi.org/10.1016/j.brain.2023.100066, URL: https://linkinghub.elsevier.com/retrieve/pii/S2666522023000047.

Steinmann, P., Hossain, M., Possart, G., 2012. Hyperelastic models for rubber-like materials: consistent tangent operators and suitability for Treloar's data. Arch. Appl. Mech. 82 (9), 1183–1217. http://dx.doi.org/10.1007/s00419-012-0610-z, URL: http://link.springer.com/10.1007/s00419-012-0610-z.

Sussman, T., Bathe, K.-J., 2009. A model of incompressible isotropic hyperelastic material behavior using spline interpolations of tension-compression test data. Commun. Numer. Methods. Eng. 25 (1), 53–63. http://dx.doi.org/10.1002/cnm.1105, URL: http://doi.wiley.com/10.1002/cnm.1105.

Tac, V., Sahli Costabal, F., Tepole, A.B., 2022. Data-driven tissue mechanics with polyconvex neural ordinary differential equations. Comput. Methods Appl. Mech. Engrg. 398, 115248. http://dx.doi.org/10.1016/j.cma.2022.115248, URL: https://linkinghub.elsevier.com/retrieve/pii/S0045782522003838.

Thakolkaran, P., Joshi, A., Zheng, Y., Flaschel, M., De Lorenzis, L., Kumar, S., 2022. NN-EUCLID: Deep-learning hyperelasticity without stress data. J. Mech. Phys. Solids 169, 105076. http://dx.doi.org/10.1016/j.jmps.2022.105076, URL: https://linkinghub.elsevier.com/retrieve/pii/S0022509622002538.

Tibshirani, R., 1996. Regression shrinkage and selection via the lasso. J. R. Stat. Soc. Ser. B Stat. Methodol. 58 (1), 267–288. http://dx.doi.org/10.1111/j.2517-6161.1996.tb02080.x, URL: http://doi.wiley.com/10.1111/j.2517-6161.1996.tb02080.x.

Wang, Z., Estrada, J., Arruda, E., Garikipati, K., 2021. Inference of deformation mechanisms and constitutive response of soft material surrogates of biological tissue by full-field characterization and data-driven variational system identification. J. Mech. Phys. Solids 153, 104474. http://dx.doi.org/10.1016/j.jmps.2021.104474, URL: https://linkinghub.elsevier.com/retrieve/pii/S0022509621001459.

Yu, H., Flaschel, M., De Lorenzis, L., 2023. Supplementary software for "automated discovery of interpretable hyperelastic material models for human brain tissue with EUCLID". ETH Library http://dx.doi.org/10.5905/ethz-1007-638.